Nanomaterials in Advanced, High-Performance Aerogel Composites: A Review

Elizabeth Barrios [1,2], **David Fox** [1,3]**, Yuen Yee Li Sip** [1]**, Ruginn Catarata** [1]**, Jean E. Calderon** [1]**, Nilab Azim** [1,3]**, Sajia Afrin** [1,3]**, Zeyang Zhang** [3] **and Lei Zhai** [1,2,3,*]

[1] NanoScience Technology Center, University of Central Florida, Orlando, FL 32826, USA;
eab143@Knights.ucf.edu (E.B.); foxd@knights.ucf.edu (D.F.); yuen-yeeli@knights.ucf.edu (Y.Y.L.S.);
Rcatarata@knights.ucf.edu (R.C.); Jean.CalderonFlores@ucf.edu (J.E.C.); nilabazim@Knights.ucf.edu (N.A.);
sajia@knights.ucf.edu (S.A.)
[2] Department of Materials Science and Engineering, University of Central Florida, Orlando, FL 32816, USA
[3] Department of Chemistry, University of Central Florida, Orlando, FL 32816, USA;
zeyangzhang@Knights.ucf.edu
* Correspondence: lzhai@ucf.edu; Tel.: +01-407-882-2847

Abstract: Aerogels are one of the most interesting materials of the 21st century owing to their high porosity, low density, and large available surface area. Historically, aerogels have been used for highly efficient insulation and niche applications, such as interstellar particle capture. Recently, aerogels have made their way into the composite universe. By coupling nanomaterial with a variety of matrix materials, lightweight, high-performance composite aerogels have been developed for applications ranging from lithium-ion batteries to tissue engineering materials. In this paper, the current status of aerogel composites based on nanomaterials is reviewed and their application in environmental remediation, energy storage, controlled drug delivery, tissue engineering, and biosensing are discussed.

Keywords: aerogel; nanocomposites; aerogel composites; energy storage; sensors; biomedical engineering; tissue engineering; graphene; cellulose; cellulose nanofibers

1. Introduction

Aerogels have become one of the most exciting materials of the 21st century. The unique processing strategy produces materials with extremely high porosities and low densities, high specific surface areas, high dielectric strengths, and low thermal conductivities [1,2]. These properties have made aerogels novel and intriguing materials for applications in aerospace, energy generation and storage, biomedical devices and implants, sensors, and coatings [2]. Since the introduction of the silica aerogel by Kistler in the 1930s, aerogels have been made out of a variety of materials including metal oxides, chalcogenides, biopolymers, and resins to name a few. More recently, aerogels have entered the realm of nanotechnology, incorporating a variety of nanomaterials into the aerogel matrix and using such materials to create composite aerogels.

While an aerogel's network contains pores with diameters on the order of nanometers, incorporating nanomaterials into an aerogel has further enhanced the functional properties of the aerogels. Since this first use of carbon nanomaterials in the production of an aerogel structure, the utilization of a variety of nanomaterials for the development of high-performance aerogel structures has grown exponentially. For example, carbon nanomaterials such as carbon nanotubes, graphene, and carbon nanofibers have been incorporated into aerogels to improve the electrical conductivity and performance for applications such as supercapacitors, sensors, and batteries [1,3]. In other earlier works,

metal chalcogenide nanoparticles were used as quantum dots to create semiconductor aerogels for photovoltaic and sensing applications [4]. In another effort, synergistic composites of nanostructured aerogels and metal oxides were fabricated using atomic layer deposition for catalytic membranes and gas sensors [5].

In this review, recent trends regarding the fabrication and utilization of nanomaterials in high-performing composite aerogels are discussed. General aerogel fabrication schemes are outlined first, including a review on the fabrication of aerogels via 3D-printing techniques. Next, 1D and 2D nanomaterials commonly used for the synthesis of composite aerogels are discussed, including the nanomaterial's fabrication schemes. Finally, the application of aerogel composites of nanomaterials in environmental remediation, energy storage, controlled drug delivery, and tissue engineering are discussed.

## 2. Aerogel Fabrication Strategies

The preparation of aerogels typically involves three distinct steps: (1) the sol-gel transition (gelation), (2) the network perfection (aging), and (3) the gel-aerogel transition (drying). Once the desired materials are selected for the fabrication of the aerogel, the precursor materials are dispersed in a liquid (i.e., colloidal dispersion) and allowed to gel, thus forming a continuous network of solid particles throughout the liquid [6]. For some materials, the transition from a colloidal dispersion into a gel happens without the addition of crosslinking materials [7]. For others, crosslinking materials are added to the dispersion to promote the strong interaction of the solid particles in order to form the gel [8,9]. The gelation time depends heavily on a variety of factors such as the chemical composition of the precursor solution, the concentration of the precursor materials and additives, the processing temperature, and the pH [8,10–13]. Many materials may require additional curing after gelation (i.e., network perfection) in order to strengthen the aerogel network [8,14–18]. Once the gelation is completed, the gel is dried in such a way as to minimize the surface tension within the pores of the solid network. This is typically accomplished through supercritical fluid extraction using supercritical carbon dioxide (scCO$_2$) or freeze-drying (Figure 1a,b). More recently, the aerogel fabrication scheme has been revolutionized in order to create 3D-printed aerogels (Section 2.3). This section briefly describes and compares the processing strategies of supercritical drying, freeze-drying, and 3D printing.
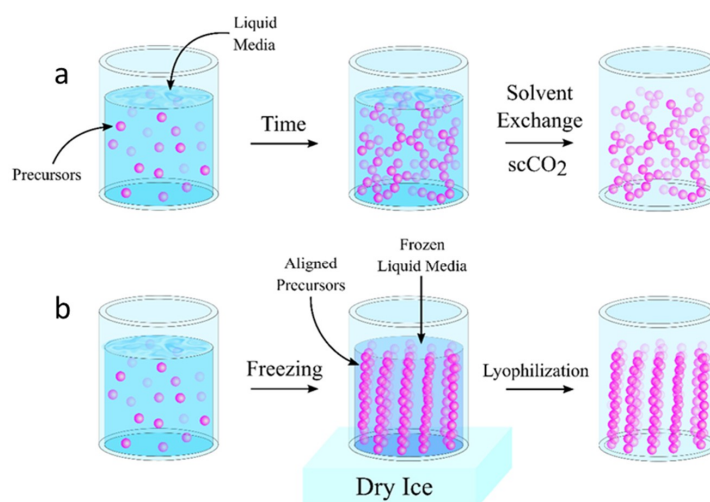
Figure 1. Comparison of aerogel fabrication strategies showing typical transitions into an aerogel. (**a**) shows the supercritical drying process where precursor materials undergo gelation prior to supercritical drying. Often, these processes include a solvent exchange step after gelation to provide better fluids for supercritical drying. (**b**) shows a standard freeze-drying technique where an aqueous solution is frozen and the ice crystal formation dictates the alignment of the precursor materials and thus, the resulting pore structure of the dried aerogel.

2.1. Supercritical Drying

To dry the gel, while preserving the highly porous network of an aerogel, supercritical drying employs the use of the liquid-gas transition that occurs beyond the critical point of a substance (Figures 1a and 2). By using this liquid-gas transition that avoids crossing the liquid-gas phase boundary, the surface tension that would arise within the pores due to the evaporation of a liquid is eliminated, thereby preventing the collapse of the pores [6]. Through heating and pressurization, the liquid solvent reaches its critical point, at which point the liquid and gas phases become indistinguishable. Past this point, the supercritical fluid is converted into the gaseous phase upon an isothermal de-pressurization. This process results in a phase change without crossing the liquid-gas phase boundary. This method is proven to be excellent at preserving the highly porous nature of the solid network without significant shrinkage or cracking. While other fluids have been reported for the creation of supercritically dried aerogels, scCO$_2$ is the most common substance with a relatively mild supercritical point at 31 °C and 7.4 MPa. CO$_2$ is also relatively non-toxic, non-flammable, inert, and cost-effective when compared to other fluids, such as methanol or ethanol [19]. While being a highly effective method for producing aerogels, supercritical drying takes several days, requires specialized equipment, and presents significant safety hazards due to its high-pressure operation.
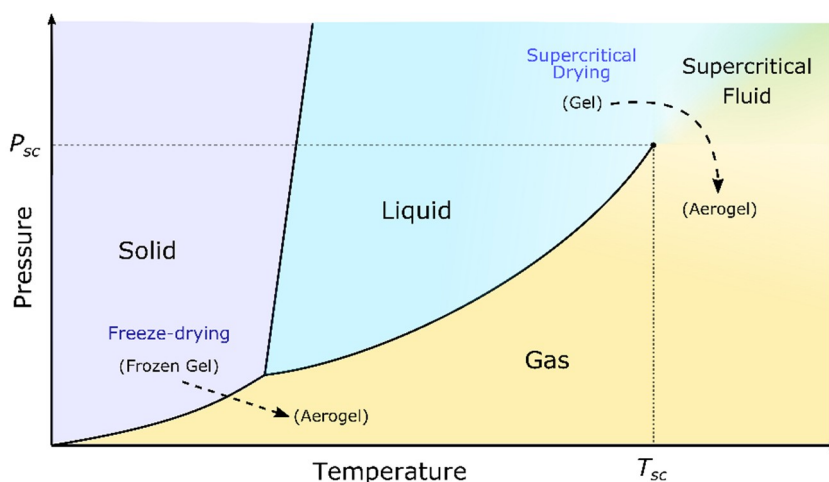
Figure 2. A typical phase diagram for pure compounds. Two methods are shown for the gel to aerogel transition, indicated by I → II. The solid-gas transition depicts the transition from a frozen gel (I) to the dried porous gel (II) during freeze-drying (Section 2.2). The transition from a liquid to gas during supercritical drying requires a rise in temperature and pressure (curved arrow from I → II) to avoid crossing the liquid-gas phase boundary (Section 2.1). This pass into the supercritical region eliminates surface tension and capillary forces.

2.2. Freeze-Drying

Freeze-drying, also known as freeze-casting or ice-templating, offers an alternative to the high temperature and high-pressure requirements of supercritical drying. Additionally, freeze-drying offers more control of the solid structure development by controlling the ice crystal growth during freezing (Figure 1b) [20–23]. In this method, a colloidal dispersion of the aerogel precursors is frozen, with the liquid component freezing into different morphologies depending on a variety of factors such as the precursor concentration, type of liquid, temperature of freezing, and freezing container [21–23]. As this liquid freezes, the solid precursor molecules are forced into the spaces between the growing crystals. Once completely frozen, the frozen liquid is sublimed into a gas through lyophilization, which removes much of the capillary forces, as was observed in supercritical drying (Figure 2) [24,25]. Though typically classified as a "cryogel", aerogels produced through freeze-drying often experience some shrinkage and cracking while also producing a non-homogenous aerogel framework [6]. This often leads to

freeze-drying being used for the creation of aerogel powders or as a framework for composite aerogels, as will be discussed in Sections 3 and 4 of this review [26–30].

2.3. 3D Printing

The three-dimensional printing (3DP) of aerogels is revolutionizing the field by enabling a fast and accurate fabrication of complex 3D porous structures, thereby introducing new functionalities, lower costs, and higher reliability in aerogel manufacturing [31,32]. 3DP, in general, is a type of additive manufacturing technique that builds 3D objects through a layer-by-layer growth process [33,34]. This technique makes it possible to fabricate highly customizable and complex structures for many industrial sectors in significantly reduced times while using a variety of materials such as polymers, ceramics, and metals [32,34]. The 3DP of aerogels is considered a hybrid fabrication technique to produce extremely lightweight 3D structures, employing new depositional strategies for the creation of the 3D gel constructs while utilizing the common drying methods of supercritical drying and freeze-drying, as discussed previously.

3DP of aerogel techniques are categorized depending on the sol-gel transitions during the printing process. These categories include: (1) direct ink writing (DIW), where a gel is formed prior to printing [35]; (2) stereolithography (SLA), where the sol-gel transition occurs during printing [36]; and (3) inkjet printing (IJP), where the sol-gel transition occurs after printing (Figure 3) [37]. SLA is a technique that prints 3D structures using photocurable materials through a process called photopolymerization, in which polymer layers solidify upon exposure to specific laser wavelengths (Figure 3a). IJP is a non-contact, droplet-based material deposition process, with the potential to be modified to deposit photocurable materials to achieve patterning with high resolution (Figure 3b). DIW is an extrusion-based printing technique that involves the deposition of continuous ink filaments, in a layer-by-layer fashion, to realize the 3D constructs (Figure 3c).
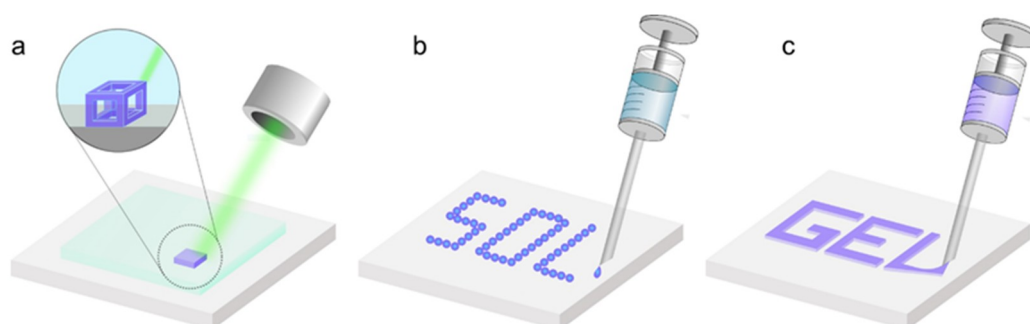
Figure 3. Schematic depiction of the three main 3D-printing techniques employed for the fabrication of aerogels. (**a**) Stereolithography, where a laser is used to transform the sol to a gel during the printing process; (**b**) ink-jet printing, where a solution is printed into its desired structure prior to observing gelation; and (**c**) direct ink writing, where the gel is formed prior to printing and the gel is extruded in order to achieve the desired structure.

Similar to the traditional aerogel synthesis techniques, the 3D printing of aerogels comes with its own limitations. For instance, SLA requires the use of only photocurable materials, whereas DIW and IJP offer a lot more versatility when it comes to material selection. SLA often requires expensive accessories, masks, and tools, whereas DIW and IJP do not. However, DIW and IJP both suffer from nozzle blockage caused by nanofiller clusters or high viscosity materials, which is not observed in SLA techniques. SLA provides the advantage of rapid gelation, which is desirable as gelation is known to be time consuming, with some materials requiring significant curing (i.e., aging) in order to produce a structurally sound gel [33]. DIW methods do not offer such rapid gelation; however, it is the most common 3DP technique for aerogels. IJP is a unique technique known for its novelty, simplicity,

and ability to fabricate highly modified 3D aerogels as demonstrated in studies discussed later in the review.

As an example of 3DP, silica aerogels were produced through SLA [38] where gels were 3D printed by illuminating photosensitive precursor solutions with a green laser beam (λ = 532 nm). Gelation of the precursor solutions containing an alkoxy-silane, a monomer, and a visible-light photoinitiator (Eosin Y) were triggered, not by the heat from the laser, but by the heat produced from polymerization. The internal heat evolution from the polymerization of the monomer (hexadiodiacrylate) overcame the activation energy for the condensation reaction of the alkoxy-silane (teteraorthosilicate), consequently forming a silica network. The gel was then supercritically dried, leaving behind a polymer crosslinked silica aerogel. Although the drying methods were conventional, the laser induced rapid gelation process added the benefit of ease in fabrication by cutting down the time required for gelation. A similar sol modification followed by SLA has realized hybrid constructs with crosslinked hexagonal honeycomb structures and aerogel cores [39]. These modifications of the sol prior to gelation is a common theme in the fabrication of 3D printed aerogels. In some cases, the use of nanomaterials can mitigate issues that occur when a material is not directly printable using 3D printing technologies [35]. In other cases, the incorporation of nanomaterials into 3D printed aerogels can create aerogels with optimized properties and added functionalities [35]. The following sections will provide details regarding the use of nanomaterials in the 3D printing of aerogel macrostructures.

3. Nanostructured Materials for Aerogel Fabrication

One- and two-dimensional nanostructured materials such as carbon nanotubes and graphene have been used as building materials for aerogels. These nanoscale materials not only have large surface areas that provide sufficient contact to form scaffolds of aerogels, but also have intriguing properties (e.g., electrical conductivity, mechanical stability, thermal stability, etc.) that grant functionalities to aerogels.

3.1. One-Dimensional (1D) Nanomaterials

Since the first use of carbon nanotubes to modify silica aerogels in the early 2000s, many one-dimensional (1D) nanomaterials have been used extensively to develop the next generation of aerogels with improved mechanical, electrical, and chemical properties for outstanding performance in a variety of areas. Within this realm of aerogel production, nanocellulose, carbon nanotubes, and carbon nanofibers are the most intriguing 1D nanomaterials. This section details the fabrication and usage of such 1D nanomaterials for the fabrication of aerogels. Where appropriate, their use in the 3DP of aerogels is also discussed.

3.1.1. Carbon Nanotubes

Since the first production of carbon nanotubes (CNTs) in 1991 by Iijima, intense research has been done to understand their physical and structural properties, and to understand how to utilize CNTs for a variety of applications [40]. CNTs are carbon allotropes, with sp^2 hybridized carbon atoms arranged into tubes [41]. These tubes can be single-walled (SWCNTs) or composed of multi-walled tubes of concentric rings (MWCNTs). Remarkable electronic properties have been exhibited in CNTs, such as a lack of the skin effect [42], current capacities reaching 10^9–10^{10} A/cm^2 [43], and ballistic electronic transport in metallic CNTs [42,44]. SWCNTs can be semi-conductive or metallic depending on their chiral angles and diameters [45]. CNTs also exhibit excellent mechanical properties such as low densities (0.28–2 g/cm^3) [46], high tensile strengths of up to 63 GPa [47], stability at elevated temperatures (up to 700 °C in ambient atmosphere) [43], and elasticity [48]. Additionally, CNTs are known to possess relatively high resistance to oxidation, requiring treatment with strong acids and high temperatures to break the π-conjugation on the nanotube surface [49]. Their synthesis is abundantly sourced, as their precursor materials are carbon-based [50].

CNTs have found great use as components and fillers in many composite systems, where the excellent properties of CNTs can be preserved and utilized for a variety of applications [51,52]. Formation into aerogels can utilize their unique properties and surface area. To go through the typical freeze-drying or supercritical drying processes of aerogel formation, the CNT solution must first form a gel. CNTs possess a high surface area and easily aggregate in solutions. Therefore, modifying the nanotube surface is necessary for a gel network to form [53]. The modification can be non-covalent, by coupling through π–π interactions with conjugated polymers, surfactants, or other nanomaterials like graphene oxide [54]. Reports as early as 2007 showed a stable gel formation by dispersing CNTs with sodium dodecylbenzene sulfonate (NaDDBS) surfactant via bath sonication [55]. The benzene ring of the surfactant interacts with the CNT surface and the sulfonate group disperses the CNTs into the solvent. For some of the samples, the as-formed gel was placed in a 1 wt% polyvinylalcohol (PVA) aqueous solution to remove the residual surfactant and deposit PVA into the gel. Incorporation of PVA was found to reinforce the final aerogel structure. Both supercritical drying and freeze-drying were used to form these aerogels. This early system achieved conductivities of 10^{-2} S/cm in their composite systems. Additionally, these aerogels were formed with between 10–60 mg/cm^3 of CNTs, much higher than that of later studies.

CNTs are generally functionalized through a covalent bond formation between carbons on CNTs and other functional groups. The breaking of C–C bonds on CNTs may detrimentally affect the electrical conductivity and mechanical properties. Zou et al. have utilized the non-covalent π–π interactions between poly(3-hexylthiophene)-b-poly(3-(trimethoxysilyl) propyl methacrylate) (P3HT-b-PTMSPMA) and CNTs to produce CNT dispersions in chloroform. The P3HT forms a strong interaction with the CNT conjugated surface, and the PTMSPMA disperses nanotubes into the solvent. The subsequent hydrolysis and condensation of trimethoxylsilyl groups in PTMSPMA introduced strong and permanent chemical bonding between CNTs, leading to a CNT wet gel. A standing MWCNT aerogel monolith with a density of 4 mg/cm^3 was obtained after the liquid component was removed from the MWCNT wet gel (Figure 4a). The MWCNT aerogel had an ordered macroporous honeycomb structure with straight and parallel voids in 50–150 μm separated by less than 100 nm thick walls (Figure 4b,c). The aerogel has a surface area of 580 m^2/g, which is much higher than that of pristine MWCNTs (241 m^2/g). Despite the ultra-low density, the MWCNT aerogels had excellent compression recoverable property and electrical conductivity of 0.67 S/cm [56].
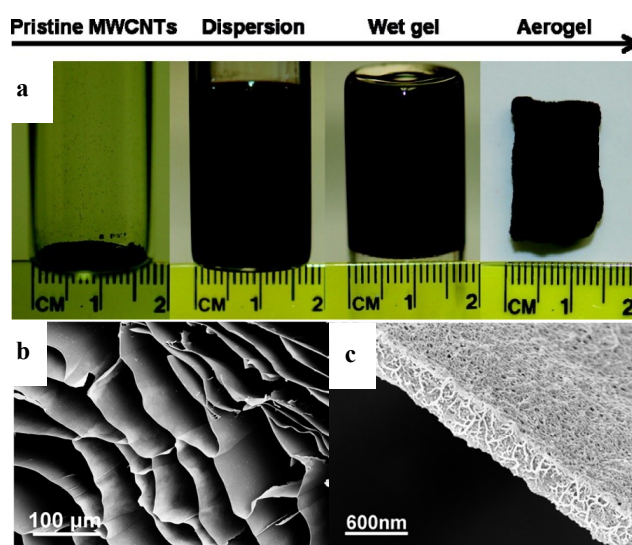
Figure 4. (**a**) Fabrication of CNT aerogels using (P3HT-b-PTMSPMA), (**b**) scanning electron microscopy (SEM) image of the macroporous honeycomb structure of the aerogel with ~100-nm-thick walls, and (**c**) SEM image of the aerogel walls with entangled CNTs. Reprinted from [56] with permission, copyright American Chemical Society, 2010.

Composite aerogels of CNTs with other nanomaterials such as graphene oxide (GO) have been shown to improve their mechanical properties [54,57]. Peng et al. generated aerogels of GO with and without CNTs [54]. They utilized the hydrothermal method, heating aqueous dispersions for 12 h at 180 °C in a Teflon-lined autoclave. The hydrothermal method partially reduces the GO and the loss of oxygen-containing functional groups restores some conjugation to the GO structure, which produces strong π–π interactions between the CNTs and GO. The pure GO structures deform permanently once loaded to a strain of 25%. With the addition of CNTs, the aerogels can bear a strain load of 80% with full structural recovery. GO-based aerogels have performed well for many applications, and a further discussion of GO-based aerogels can be found in Section 3.2.1.

Another method for modifying the CNT surface is through a direct chemical modification followed by crosslinking with other materials. While CNTs possess good chemical resistance, direct modification can be achieved through the use of strong oxidizing or reducing agents to generate reactive sites on the nanotube surface [49]. This enables crosslinking between CNTs and other components within the solution. These reactive sites also provide a site for further modification. De Marco et al. utilized a reduction scheme to crosslink the SWCNTs to each other, generating a network [58]. A one-pot reaction of sodium/naphthalene in *N,N*-dimethylacetamide (DMAc) produced negative charges on the surface of the tube, with *p*-Diiodobenzene crosslinking the SWCNTs. A low mass density of 2.3 mg/cm^3 was achieved with conductivities up to 9.4 S/cm. These oxidized surface sites can also act as a site for surface-initiated polymerization, resulting in composite materials of CNTs covalently bound to polymer chains prior to gel formation, such as the polyimide system demonstrated by Zhu et al. [59]. Concentrated acid was used to generate carboxylic acid groups on the surface, and treatment with thionyl chloride grafted material, formed the acyl chloride. Further treatment by 4,4′-Oxydianiline (ODA) produced an amine in the surface. The functionalized CNTs were added to a polymerization reaction between 3,3′,4,4′-biphenyltetracarboxylic dianhydride (BPDA) and ODA, and the ODA attached to the nanotube surface would crosslink with the growing polymer chains. Finally, chemical imidization and supercritical drying produced the composite material. Pure polyimide aerogels were found to have Young's modulus of 2.5 MPa, which was improved 292% to 9.8 MPa with the addition of 0.5 wt% CNTs to the composite.

Lightweight, high-performance CNTs in the form of aerogels and porous scaffolds benefit from a composite-based system, providing access to many materials not otherwise observed [50,56]. Strong forces can result in the irreversible deformation and collapse of monolithic structures; an effective approach has been to incorporate polymers and other nanomaterials to generate high-performance CNT aerogel composites [60]. This has been achieved through various methods, which generate non-covalent and covalent bonds between the composite materials. These structures take advantage of the natural properties of the CNTs in addition to their increased surface area. CNTs can also improve the mechanical and electrical properties of other aerogel systems, especially with other nanomaterials where synergistic effects are observed. For example, their addition into a composite system with other low dimensional materials, such as sheets of 2D graphene oxide, helps to prevent re-stacking of the sheets and improve the mechanical properties [61]. While this section has covered CNT aerogel formation and methods to improve their properties, later sections cover CNTs in composites systems for several applications. Their incorporation into varying aerogel systems has produced functional materials capable of chemical and bio-sensing [62], strain sensing [63], microwave absorption [64], separation of oil-in-water emulsions [65], sorptive structures for dyes and oils [66,67], supercapacitors (Section 4.2.1), lithium ion batteries (Section 4.2.2), hydrogen evolution [68], solar cells [69,70] among other applications not listed.

3.1.2. Nanocellulose

The first nanocellulose aerogel was demonstrated by Pääkkö et al., where a solution of cellulose nanofibers was formed into a gel and freeze-dried to fabricate aerogel structures. The resulting aerogel had a porosity of 98.7% and exhibited better mechanical properties compared to its macroscopic

counterpart [71]. Cellulose-based nanomaterials (nanocellulose) can provide a completely bio-friendly, biodegradable, and renewable material for the development of many carbon-based nanomaterials including aerogels [72–74]. The advantage of using nanocellulose is based on its high abundance and renewability in addition to its excellent mechanical properties and ease of surface modification [74,75]. In addition, the morphology and structure of nanocellulose vary depending on the cellulose source and the processing parameters [75,76]. This makes nanocellulose a valuable material for the production of aerogels and aerogel-based composites tailored for specific applications. When compared to traditional cellulose materials, nanocellulose has a higher crystallinity and aspect ratio, resulting in very low shrinkage (<7%) when fabricated as a highly porous aerogel [72]. However, during the drying process, nanocellulose is often prone to self-agglomeration, slowing the advancement of nanocellulose in the fields of aerogel and aerogel composite development [77].

As mentioned before, the structure of nanocellulose is highly variable and depends on the source of the cellulose and the processing parameters. For example, nanocellulose can be extracted from either plants or animal sources such as sea tunicates [74,78], wood pulp [76], and *Miscanthus x Giganteus* [79]. Based on the preparation process, nanocellulose is usually divided into two groups: (1) cellulose nanocrystals (CNC) and (2) cellulose nanofibrils (CNFs) [80]. The production of CNCs is typically the result of acid hydrolysis [80]. Traditionally, this process uses sulfuric acid to produce sulfonated CNCs; however, other acids have been used to produce CNCs with other surface functional groups. The production process of CNFs, however, usually requires chemical pretreatment followed by mechanical stimulation such as homogenization, micro-fluidization, or super-grinding [81]. Acid hydrolysis yields CNCs with a diameter of only a few nanometers and a length of 10–500 nm. However, the chemical and mechanical treatment of CNFs result in nanocellulose materials with a significantly lower aspect ratio with diameters on the order of 3–50 nm and only be a few micrometers long [75].

In addition to CNCs and CNFs, there is a third type of nanocellulose known as bacterial cellulose (BC), which is formed though microbial fermentation [73,82]. Compared to plant-based cellulose, bacterial cellulose has a higher degree of polymerization (>80%) [72]. Bacterial cellulose is secreted by some of the bacteria in the genera *Acetobacter, Argobacterium, Alcaligenes, Pseudomonas, Rhizobium,* and *Sarcina* [83]. By adjusting the bacterial strain and constituents in the culture medium, the structure of the BC nanofiber can be altered and developed for specific applications [84].

The fabrication of nanocellulose aerogels begins with the formation of a hydrogel. The gel formation is assisted by a large number of hydroxyl groups native to the cellulose that allow for crosslinking free of a crosslinking agent. The high stability of the gel is due to the physical crosslinks attributed to the hydrogen bonds. After gelation is achieved, the gel is then dried either through freeze drying or supercritical drying [72]. Many studies have utilized this method to produce nanocellulose aerogels for applications such as food packaging, thermal insulation, catalyst systems, shape memory aerogels, drug release, tissue engineering, and supercapacitors [77,81,85–89].

Nanocellulose is also a candidate for the 3D printing of aerogels, specifically due to the high Young's modulus and inherently low density [74,75,90]. In one study, CNC-based aerogels were 3D printed through DIW methods, where computer aided design (CAD) limitations, gel formulations, processing parameters, and nozzle tips were explored to optimize the printing process [90]. As shown in Figure 5, aerogels with a dual-pore structure were obtained. Structural pores from the printing process had an average size of 600 μm while the pores from the aerogel fabrication ranged from 20 to 800 μm. Additionally, a variety of macrostructures such as an octet cube, a pyramid, a hexagonally twisted vase, a nose model, an ear model, and a honeycomb pattern were fabricated in the aerogels, demonstrating the high flexibility of this printing technique. Little shrinkage or network damage was observed after freeze-drying, likely due to the high Young's modulus and strong hydrogen bonding between the CNCs. The dual-pore structures shown in this work demonstrated the applicability of such a technique for novel tissue engineering approaches, where the novel scaffolds could provide easy nutrient and oxygen transport, thereby promoting proliferation of cells throughout the entire structure.
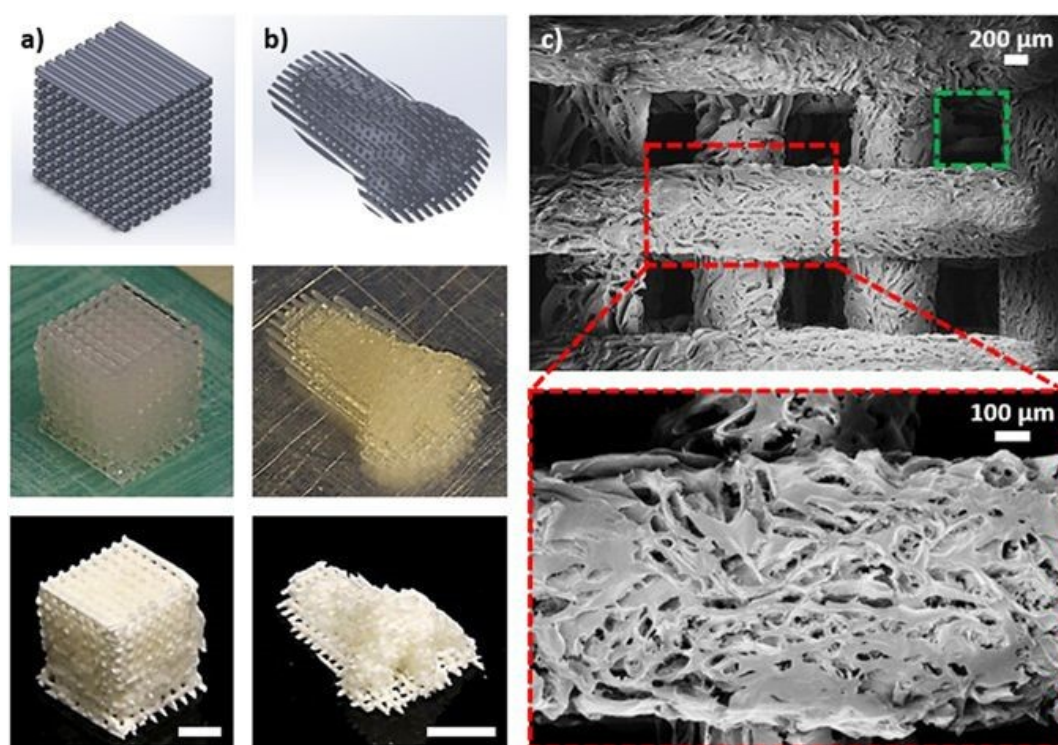
Figure 5. The DIW of aerogels in two distinct macrostructures, (**a**) a cube and (**b**) an ear. (**c**) The structural porosity, accounting for pores in the range of 600 µm (green box) and the aerogel porosity, accounting for pores in the range of 20 to 800 µm. Reprinted from [90] under open access license.

CNFs are longer, thicker, and softer than CNCs, allowing the material to form deformable networks through physical entanglements and hydrogen bonding. However, the disadvantage of CNF is the inability to be homogeneously dispersed for DIW processing. To address this limitation, Li et al. modified the surface of CNFs with tetramethyl-1-piperdinyloxy (TEMPO), giving TEMPO-functionalized CNFs (T-CNF). The chemically modified T-CNF was defibrillated due to the increased surface repulsive charge of individual fibers, rendering it processable as a printable ink for DIW constructs [91]. The carboxylic groups of the T-CNF facilitated Kymene crosslinking, creating an interpenetrating network of T-CNF and polymerized Kymene. This allowed the aerogel to maintain structural integrity both under water and under an applied force. The average Young's modulus of un-crosslinked T-CNF aerogels was 2.1 ± 0.1 MPa and was found to increase to 3.2 ± 0.2 MPa after crosslinking. Using this method, the CNF-based ink was able to accurately and reproducibly print 3D structures. In addition, post-processing of the printed CNF aerogels demonstrated improved mechanical and chemical properties of the final aerogel.

Another study of CNF aerogels explored the post-processing and drying of CNF gels after printing [92]. The CNF hydrogels contained 2 wt% cellulose (98 wt% water) and were printed via DIW. The printed grid cube was strong enough to support itself; however, the cube was transferred to a $CaCl_2$ bath in order to reduce the surface charge of the fibrils, thereby allowing the crosslinking of the fibrils with one another, consequently increasing the strength of the structure. The structures were then dried by one of four different methods: (i) air drying, (ii) air drying in the presence of surfactants, (iii) solvent exchange before drying, and (iv) freeze drying, as depicted in Figure 6. The freeze-dried method exhibited a highly porous structure without much shrinkage or distortion of the original structure, whereas the air-died aerogel collapsed in the z-direction (Figure 6b). When tested for mechanical robustness, it was found that the freeze-dried aerogels had a tensile strength of 3.9 ± 2.7 MPa and a mean stiffness of 0.031 ± 0.019 GPa. The rest of the printed cubes were dried in air and had a mean ultimate tensile strength of 114 ± 14 MPa and mean stiffness of 4.3 ± 0.3 GPa. When dried in air in the

presence of surfactants, the printed cubes resulted in significant shrinkage, but still managed to retain their 3D structures due to homogenous drying. The solvent exchange study was performed so that a less polar liquid than water could retain the structure as it is air-dried; however, the cubes resulted in similar shrinkage as for the surfactant method. Additionally, they found a large difference in the surface structures of the gels between fast and slow drying, where ice crystal growth has an effect on the timescale of particle rearrangement. They found that slow freezing produced rougher surface and fast drying resulted in dimensional stability. Ultimately, this study shows the versatility in tuning CNF aerogel properties, even after print, by controlling the post-processing and drying process.
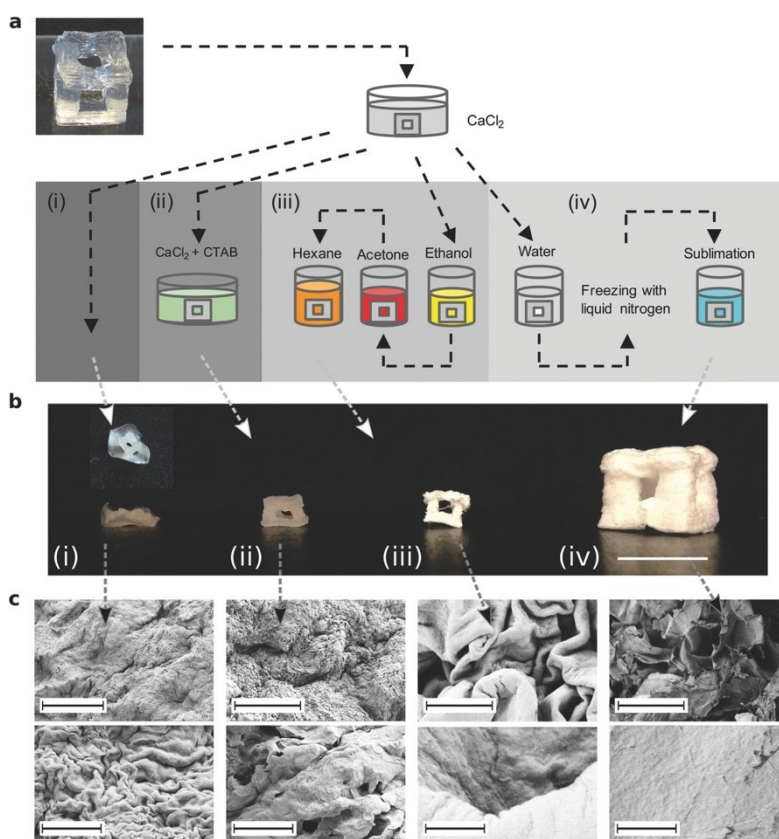
Figure 6. Depiction of the DIW of CNF aerogels (**a**) and four different methods of drying (**b**). From left to right, the CNF hydrogel drying procedures are (i) air drying), (ii) air drying in the presence of surfactants, (iii) solvent exchange before drying, and (iv) freeze-drying. (**c**) SEM micrographs of the resulting microstructures of such dried CNF aerogels. Adapted from [92] with permission, copyright John Wiley & Sons, 2016.
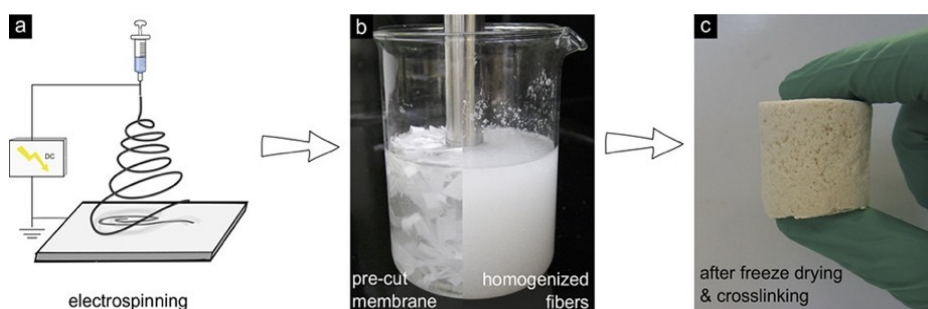
3.1.3. Nanofibers

Nanofibers are slender, elongated thread-like structures with nanoscale-sized diameters. These structures hold many advantages, such as excellent mechanical performance, small aperture, tunable porosity, and high surface area to unit mass ratio [93,94]. Additionally, nanofibers can be produced from a wide selection of polymers, all with different physical properties, leading to the ability to tailor the nanofiber for use in specific applications [94]. Nanofibers can also be coupled with other compounds and nanostructures to introduce novel and enhanced properties to nanostructured materials [93].

Many methods, including drawing, phase separation, template synthesis, self-assembly, melt-blowing, biocomponent extrusion, force-spinning, and electrospinning, have been used to produce nanofibers [95–100]. Drawing involves a micromanipulator which touches a polymer liquid droplet and draws out a single nanofiber [95]. Phase separation into a fibrous macro-structure is applicable only

in certain polymers such as nanocellulose, which was discussed in Section 3.1.2. Template synthesis uses unique templates or membranes that contain nanopores in order to extrude nanofibers when pressure is applied to the template [96]. Self-assembly involves building very fine fibers from smaller molecules and is common to form peptide-amphiphile nanofibers [97]. These methods are often used for the lab-scale synthesis of nanofibers due to their low rate of producing nanofibers. For large-scale industrial applications, melt-blowing, biocomponent extrusion, force-spinning, and electrospinning are often used. Biocomponent extrusion, also known as islands-in-the-sea, uses a melt blend of two immiscible polymers to spin a bicomponent blended fiber with an island-in-the-sea morphology [98]. Force-spinning, or centrifugal spinning, utilizes force to pump the polymer solution out of an orifice that is rotating at high speeds to create a large amount of long, stretched fibers (similar to a cotton candy machine) [99]. Melt-blowing involves extruding or blowing out the polymer melt by blowing high-speed gases out of small nozzles [100].

While all of these aforementioned methods are utilized extensively in the production of nanofibers, electrospinning is the method utilized the most for nanofiber production due to its low cost, high versatility, robustness, and high throughput compared to the other techniques [93,94]. Drawing, template synthesis, and self-assembly are limited to laboratory usage due to its low production rate and thus can be challenging to get large dispersions of nanofibers for macro-structure fabrication such as aerogels [99]. Even higher throughput routes such as melt-blowing, bicomponent extrusion, and force-spinning are limited in polymer selection and require expensive equipment [99]. Electrospinning is an electro-hydrodynamical process that is composed of two stages: jet formation and fiber stretching (Figure 7) [94]. First, an electrical field is applied to a polymer solution which results in the sharpening of a droplet into a cone shape followed by an inversion stage where a fiber jet is formed [94]. As the jet travels to the collector, the charges within the fiber matrix repel each other causing bending instabilities. These bending instabilities stretch the fibers yielding structures with nanometer sized diameters [94]. This results in the large production of continuous polymer fibers and fibers with various configurations such as core-shell and hollow fibers due to the selection of nozzle equipment [101].

Figure 7. The processing schematic of aerogel fabrication via the electrospinning of nanofiber mats. Reprinted from [102] with permission, copyright American Chemical Society, 2018.

Creating an aerogel out of nanofibers enhances the specific surface area, improves the mechanical properties, and promotes innovative functionality in the aerogel structure. To produce the nanofibrous aerogels, supercritical drying or freeze-drying is performed on dispersions containing single nanofibers or nanofiber mats obtained from electrospinning. When making aerogels out of nanofiber mats, the mats are often cut into smaller fragments through sonication (i.e., dispersion cut) prior to aerogel formation [102]. One example of an aerogel derived from a single-nanofiber dispersion is the freeze-drying of a native or 3D-printed cellulose nanofibril gel dispersion, which was discussed in Section 3.1.2. In another work, a composite aerogel was fabricated by freeze-drying a homogeneous solution of electrospun SiO_2 nanofibers, polyacrylamide, and aluminoborosilicate (AlBSi) [103]. During the freezing of the composite solution, the nanofibers gathered along the edges of the ice-crystals, giving a hierarchical lamellar structure in the final aerogel, differing from the typical circular porous structure

found in other ceramic aerogels. Calcination of the aerogel removed the organic component, cementing the nanofibers within the network, and creating the amorphous SiO_2 nanofiber-AlBSi ceramic aerogel. The resulting ceramic aerogel was found to have an ultralow density (0.15 mg/cm^3), a porosity of 99.993% with pores ranging from 100–1000 nm, and a high elasticity. Interestingly, this aerogel was also found to be flame resistant. In another example, nanofiber mats composed of pullulan and poly(vinyl alcohol) were dispersion cut and freeze-dried to create a composite aerogel [102]. The porosity of the aerogel was found to be tunable as a higher volume fraction of nanofibers caused a decrease in the porosity of the aerogel. Additionally, more than one type of nanofiber mat can be combined during homogenization to provide different compositions and properties of the resulting aerogels. For example, one research group homogenized a mixture of two types of electrospun mats, polyacrylonitrile/bifunctional benzoxazine (PAN/BA-a) and SiO_2 [104]. The dispersion of nanofiber mats was freeze-dried and crosslinked in situ in order to obtain a stable, hybrid aerogel comprised of both organic and inorganic nanofibers. The density can be tuned in the range of 0.53–9.6 mg/cm^3 by varying the concentrations of the starting nanofiber dispersions. When tested in strain, such an aerogel was found to have a maximum stress value of 10.6 kPa (first elastic regime) while showing a strain of 36.1 kPa at 80% strain.

However, there are a few shortcomings when using electrospinning techniques. Firstly, electrospinning involves the use of high voltages, introducing a significant safety concern [94]. In addition, there are many instabilities within the electrospinning process such as the lack of precise control over the polymer flow rate, electrical field, and droplet drying [101]. Consistent monitoring, safety checks, and maintenance are required to ensure consistent fiber production. Furthermore, the production rate with single-nozzle electrospinning is low and the cost per gram of such fibers is high [99]. Various groups have begun to mitigate this by utilizing multi-nozzle or nozzle-free electrospinning [93,99].

In recent attempts to mitigate the concerns of the aforementioned processing strategies, a new bottom-up approach called hydrothermal carbonization (HTC) has been used to produce nanofibers [105,106]. In this technique, organic compounds are treated in an aqueous environment at high temperatures (150–350 °C) and ambient pressures in order to form carbonaceous solid products. Qian et al. synthesized carbon nanofibers through HTC [106] where glucose was self-assembled and grown around tellurium nanofibers, which served as a structural template for the aerogel. The solution containing the glucose and tellurium nanofibers was etched and washed to remove the inorganic materials prior to being freeze-dried to obtain the desired HTC-carbon nanofiber aerogel. In another study, the HTC-carbon nanofiber aerogel was synthesized from glucosamine, a nitrogen-containing carbohydrate [107]. This resulted in the formation of a nitrogen-doped carbon aerogel with enhanced electrical conductivity (Figure 8). The main benefit of this technique over electrospinning is the ability to control the diameters of the resulting fibers. HTC has produced nanofibers with very fine diameters (minimum: 25 nm) with a narrow size distribution, resulting in smaller secondary pore sizes [108]. In addition, a high yield of the converted carbon solids is obtained using HTC [73,108]. The downside of the HTC approach is that costly tellurium nanofibers are often used to guide the growth of the carbon nanofibers [108]. Future work could utilize other materials, such as low-cost inorganic nanowires and cellulose nanofiber, for the structural template making HTC a more feasible option.
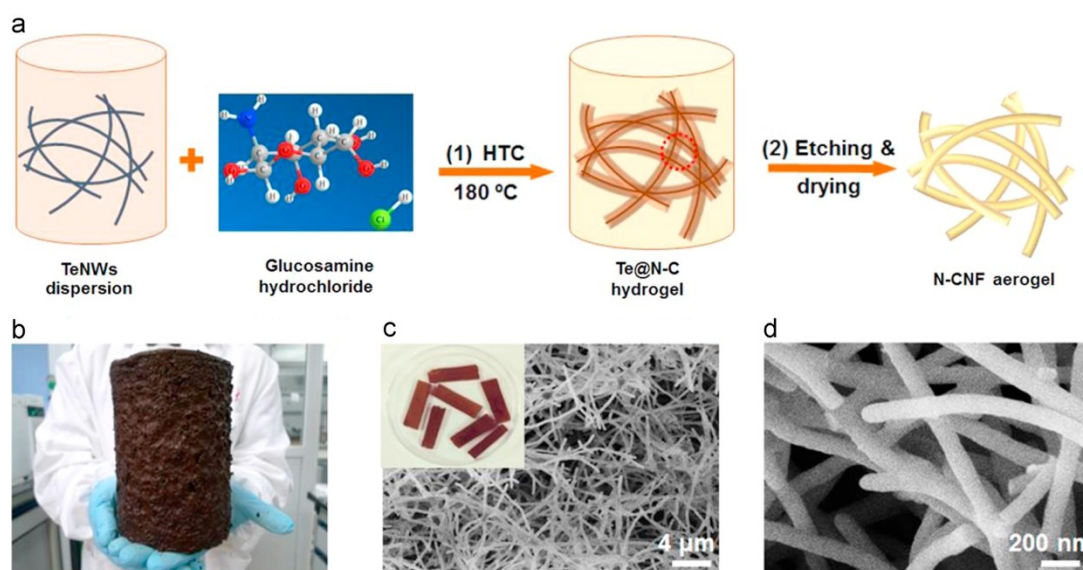
Figure 8. (**a**) HTC synthesis of nitrogen-doped carbon nanofiber aerogels; (**b**) image of large-scale quantities of such a product, and (**c**) and (**d**) SEM micrographs of images at different magnifications. Reproduced from [107], copyright Elsevier, 2015.

3.2. Two-Dimensional (2D) Nanomaterials

Two-dimensional nanomaterials have been extensively investigated for aerogel fabrication since Novoselov and Geim reported novel physical properties of graphene in 2004 [109]. Graphene and a variety of 2D nanomaterials have been recognized as an extraordinary material for the creation of lightweight, aerogel-based composites for various applications.

3.2.1. Graphene and Its Derivatives

Graphene is a one-atom-thick, hexagonal honeycomb structure of sp^2 hybridized carbon. Its unique structure yields extraordinary physical, chemical and mechanical properties. Graphene has an outstanding charge carrier mobility of 2.5×105 cm^2/V·s at room temperature, a high thermal conductivity of 3000 W/m·K, and a good optical transparency of 97.7% [110,111]. Graphene also possesses a high theoretical surface area of 2630 m^2/g, a Young's modulus of 1 TPa with a strength of 130 GPa, and a low density [112,113].

Processing of pristine graphene is quite difficult, as it cannot be dispersed in solvents due to the high aspect ratio of the graphene sheets and the strong π–π interactions [114]. To generate a graphene structure which can be easily dispersed in a variety of solvents without rapid aggregation, oxygen functional moieties are generated on edges and basal planes of graphene sheets, producing graphene oxide (GO). Functional groups, such as epoxy, hydroxyl, carbonyl, and carboxylic groups, dramatically increase the aqueous solubility of graphene and promotes the interaction with polymers and other materials [115]. Even with functional groups, GO sheets can aggregate due to π–π interactions if a solution is too concentrated, thereby losing the properties of the hydrogel. To avoid such a network collapse, GO suspensions are typically freeze-dried immediately after dispersion. For example, researchers recently demonstrated a revolutionary process to freeze-dry such GO suspensions to create a radially aligned aerogel, something that was previously not observed previously with freeze-drying techniques (Figure 9) [22]. GO-based aerogels can be reduced to recover some conjugated carbon bonds if the electrical conductivity is desired [116].

The aggregation of GO can be alleviated through compositing the GO suspensions with polymeric materials prior to the formation of the aerogel structure [117–119]. When the polymer is incorporated into the graphene system, crosslinking occurs between the polymer and graphene or its derivatives. While this interaction can happen by a variety of different mechanisms, this crosslinking transforms

the graphene-polymer solution into a gel that can be dried into the desired aerogel. On one hand, hydrogen-bonding and π–π interactions in this system can guide the crosslinking reaction, following a so-called direct self-assembly method [120]. On the other hand, reducing agents can be added to the system to promote crosslinking via covalent bonding. Different kinds of methods can be used to combine the polymer matrixes with the graphene sheets. These methods include solution mixing [121–124] and sol-gel processing [125–127]. The methods are chosen based on the properties of the polymer to be composited with the graphene. Solvent mixing is the simplest, yet most widely used, method to mix a polymer with GO. A GO dispersion and a polymer solution can be mixed followed immediately by freeze-drying. The composite is then formed by the phase separation that occurs during freeze-drying. The sol-gel method of composite formation happens after the mixing of GO and polymer, where the gelation of the polymer provides an excellent base to form a hydrogel-based composite with the GO prior to freeze-drying. Combining graphene with a polymer to create a composite aerogel has a lot of advantages, leading to many applications that will be discussed in Section 4.
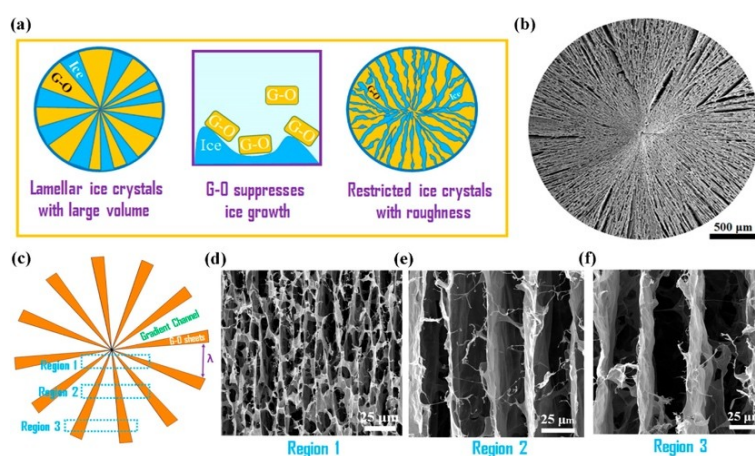

Figure 9. Schematics and images from the radially grown GO aerogels. (**a**) Illustrates the ice-templating process, (**b**) shows scanning electron microscopy (SEM) images of the radially aligned aerogel, (**c**) illustrates the decreasing width of the radial channels, which decrease from edge to center, and (**d**–**f**) show SEM micrographs of the sections outlined in (**c**). Adapted from [22] with permission, copyright American Chemical Society, 2018.

Some studies have investigated the feasibility of the 3DP (three-dimensional printing) of graphene aerogels. Such techniques would be excellent for tailoring the microarchitecture of the graphene aerogel for specific applications such as all-solid-state-batteries, micropressure sensors, flexible electrodes, and electrochemical catalyst templates [128]. In a study by Zhang et al., graphene aerogel lattice architectures were 3D printed using a modified inkjet printing (IJP) technique [37]. This 3DP method was relatively simple with only dilute aqueous GO solutions (1 mg/mL) being used as the printing material. In this IJP technique, the GO suspension was frozen by selectively solidifying the solution onto ice crystals that were grown on a cold sink cooled to −25 °C. These ice crystals were built with water droplets frozen during printing and the GO suspension was only ejected dropwise when needed. When the liquid solution was deposited on top of the previous layer, the newly deposited material melted the previous layer. The two layers mixed in this melted state and refroze together, firmly bonding the two layers to achieve the structural integrity desired. The 3D printed GO ice lattice was then immersed in liquid nitrogen for 30 min in order to achieve critical freezing and was subsequently further frozen in a freezer (−80 °C) for 24 h. This allowed for the sufficient assembly of the GO sheets. Once completely frozen, the materials were dried via freeze-drying for 48 h. Subsequent thermal treatment at 1000 °C for 30 min in an argon atmosphere reduced the GO to rGO. The use of a dilute GO suspension resulted in a very low density (0.5–19 mg/cm^3) aerogel with a larger surface area when

compared to other 3D printed graphene aerogels. The use of a multi-nozzle, drop-on-demand IJP technique coupled with freeze-drying enabled the control of both the micro- and macrostructure of the graphene aerogel. This resulted in an aerogel with high electrical conductivity of approximately 15.4 S/m, as well as high compressibility. The limitation of IJP arises as the 3D printed structure grows in the z-direction because maintaining a uniform temperature throughout the growing structure becomes increasingly difficult, which may affect the structural integrity of the final aerogel. Thus, a majority of 3D printed graphene aerogels are fabricated by DIW where a gel is obtained prior to deposition, as opposed to after deposition as in IJP.

DIW (direct ink writing) provides a technique to fabricate 3D structures continuously without external support structures, leading to the construction of more complex structures. However, the challenge of DIW is the design of the gel-based viscoelastic ink. Ideally, these inks have non-Newtonian shear thinning behavior [129] to enhance the shape retention as it facilitates the flow of the ink. As for DIW 3DP of graphene aerogels, printable graphene-based inks with a high viscosity and self-supporting shape integrity after deposition are required. Often, these are obtained by adding functional fillers or nanomaterials, such as conductive nanoparticles or nanofibers, to the graphene suspension. Zhu et al. developed a printable graphene-based ink, while maintaining the intrinsic properties of the graphene sheets [130]. In this work, the inks in this study were either gelled using the native functionality on GO or gelled using organic sol-gel chemistry. The former was achieved through the use of ammonium carbonate solution and fumed silica. The latter process was achieved by preparing a mixture consisting of an aqueous solution of resorcinol, formaldehyde, and sodium carbonate catalyst, which was then mixed with the GO suspensions and fumed silica. The main difference between these two gelation methods was the microstructure obtained after drying. The aerogel obtained via organic sol-gel chemistry resulted in a more open, less crosslinked microstructure where the graphene sheets were free to bend and buckle under compression. They also exhibited substantial recovery when the load was removed (Figure 10). Such lattices demonstrated good electrical conductivity, low densities, large surface areas, super compressibility, and stiffness when compared to bulk graphene with a similar geometric density.
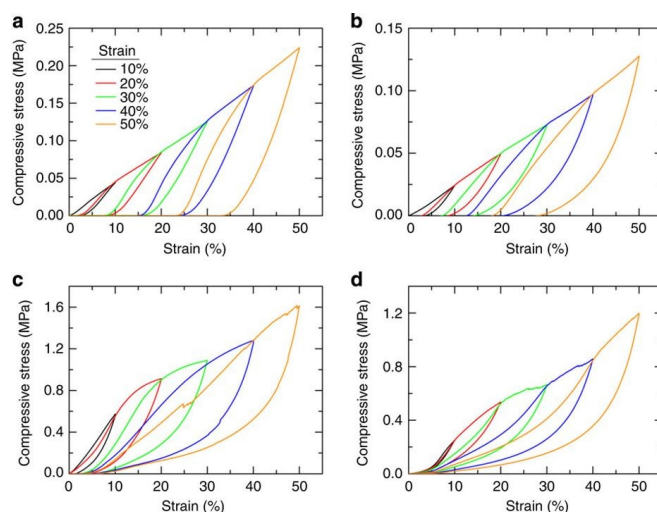
Figure 10. Reversible compressibility of various graphene aerogels created via DIW. Image (**a**) shows the behavior of a bulk graphene aerogel (31 mg cm^{-3}), (**b**) 3D-printed graphene aerogel (16 mg cm^{-3}), (**c**) bulk graphene aerogel (123 mg cm^{-3}), and (**d**) 3D-printed graphene aerogel (53 mg cm^{-3}) using resorcinol-formaldehyde. Reprinted from [130] under open access license.

Although DIW has the ability to obtain tailorable graphene aerogels, the additives required to obtain printable graphene ink lead to intercalation and weak π–π stacking among the graphene sheets. Such additives significantly hinder the mechanical and electrical properties of the resulting graphene macrostructure. Thus, rather than printing 3D graphene lattices directly, one study utilized a

template-mediated 3D printing of graphene lattices [31]. As shown in Figure 11, hollow polymer lattice architectures were designed and printed using SLA techniques. First, a photocurable polymer was used to 3D print a hollow lattice. Then, an ink mixture composed of GO and ethylenediamine (EDA) (1:3 vol. %) was injected into these hollow lattices and allowed to gel via a hydrothermal reaction (120 °C for 6 h). The gels were then freeze-dried to obtain the 3D GO aerogel/polymer composite lattice. The samples were thermally annealed (120 °C for 6 h) to decompose the polymer template. The template-mediated lattices were characterized to compare against the graphene aerogel bulk structure and was found to exhibit improved mechanical and electrical properties. The macrostructure realized by 3DP resulted in mechanical properties such as high fracture resistance. The graphene lattice had a Young's modulus around 1.05 MPa while the bulk graphene aerogels had a Young's modulus around 28 KPa. The graphene lattices also demonstrated high electrical conductivities of 0.11 and 0.81 S/cm corresponding to an aerogel density of 1.58 and 10.16 mg/cm^3, respectively. This is significantly higher than the conductivity of 0.154 S/cm at a density of 10 mg/cm^3 that was exhibited by previously reported 3D printed graphene aerogels [130,131]. This study found that implementing hydrothermal assembly of GO within stereolithography-based hollow polymer templates prevented the shrinkage of the resulting aerogel, minimized shrinkage induced fracture or collapse, and improved the electrical properties when compared to previously reported 3D printed graphene aerogels.
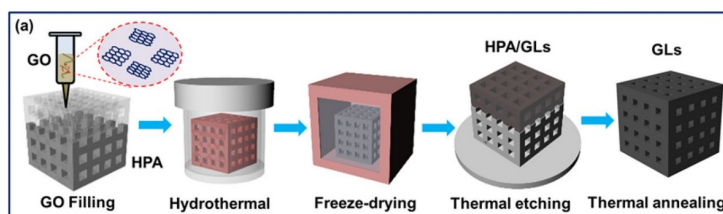
Figure 11. Schematic of 3D graphene lattice fabrication with photocurable hollow polymer architecture. Adapted from [31] with permission, copyright American Chemical Society, 2018.

3.2.2. Other 2D Materials

Although graphene shows remarkable physicochemical properties, alternative 2D materials are also of extreme interest for the creation of aerogels. While many of these materials have yet to be synthesized, hundreds of 2D materials have been predicted to be stable, such as metal disulfides, transition metal oxides, and transition metals, all with structures very similar to graphene [132]. It is apparent that such materials have a high potential for the future development of nanostructured devices and materials designed for highly specific applications. Materials such as molybdenum disulfide (MoS_2) and tungsten diselenide (WSe_2) have high stability and are relatively low in cost [133]. MoS_2 has been extensively studied for a variety of applications. They exhibit high stability and low costs; however, unlike graphene, they possess a band gap [133]. Difficulties in the preparation of pure MoS_2 scaffolds with large surface areas have been documented, but the use of graphene scaffolds has significantly mitigated this shortcoming of MoS_2 fabrication and has enabled the production of high-surface-area MoS_2 [134]. The as-generated composite structure exhibited excellent NO_2 sensing properties over pure carbon aerogels. Graphene scaffolds have a dual purpose in this composite—it serves as both a scaffold for the fabrication of high surface area MoS_2 and introduces a highly conductive network into the composite.

MoS_2 and silver (Ag) nanoparticles were integrated with graphene to obtain DIW printed hybrid graphene aerogels [135]. The XRD pattern of both of the hybrid graphene aerogels as compared to the annealed graphene demonstrated the weakening, broadening and shifting of the peak assigned to the (002) crystalline plane of graphene. The XRD results indicated that the interlayer spacing of the graphene sheets was enlarged from 0.32 to 0.42 nm, concluding that MoS_2 and Ag nanoparticles alleviated the restacking of graphene sheets. These results demonstrated the formation of a homogeneous hybrid ink composed of the inorganic additives serving as spacers to separate and support neighboring sheets.

Homogeneity of the ink significantly prevented the formation of large blocks or agglomerates to ensure higher printing precisions as well as a homogeneous distribution of additives within the final graphene aerogel network [136].

Hexagonal boron nitride (h-BN) has been attached to the single-walled carbon nanotube surfaces in a pre-fabricated carbon nanotube aerogel. The h-BN, as 2D flakes, strengthened the underlying SWCNT networks via reinforcement of the nodes between the SWCNTs, leading to a doubled Young's modulus compared to that of SWCNT networks alone. Only 0.009% volume fraction of h-BN generated mechanically robust composite aerogels that recovered their original shape even after uniaxially compressing by more than 50% [137]. Duan and coworkers have produced double-negative-index graphene/h-BN composite aerogels with robust mechanical and exceptional thermal stability [138]. First, a hierarchical porous graphene template with hyperbolic architecture was fabricated through a modified hydrothermal reduction (MHR) and noncontact freeze drying (NCFD) technique to obtain a negative Poisson's ratio (NPR) and a negative thermal expansion coefficient (NTEC) that enhanced the mechanical properties of the template (Figure 12a) [139]. h-BN was then deposited on the surface of graphene template through a chemical vapor deposition (CVD) process (Figure 12b). The resulting h-BN aerogels (h-BNAGs) had ultralow densities of less than 10 mg/cm^3 with the lowest density being 0.1 mg/cm^3 (Figure 12c). The ultralow density was attributed to the highly porous structure with h-BN layers on graphene aerogel templates (Figure 12d). Thermal etching of graphene templates from the h-BN/graphene sandwiched hybrids produced double-pane wall structures (Figure 12e). Such rational designed h-BN aerogels had near-zero strength loss after sharp thermal shocks (275 °C per second) or intense thermal stress at 1400 °C, and ultralow thermal conductivity in vacuum [~2.4 milliwatts per meter-kelvin (mW/m·K)] and in air (~20 mW/m·K), providing an ideal system for thermal superinsulation under extreme conditions.
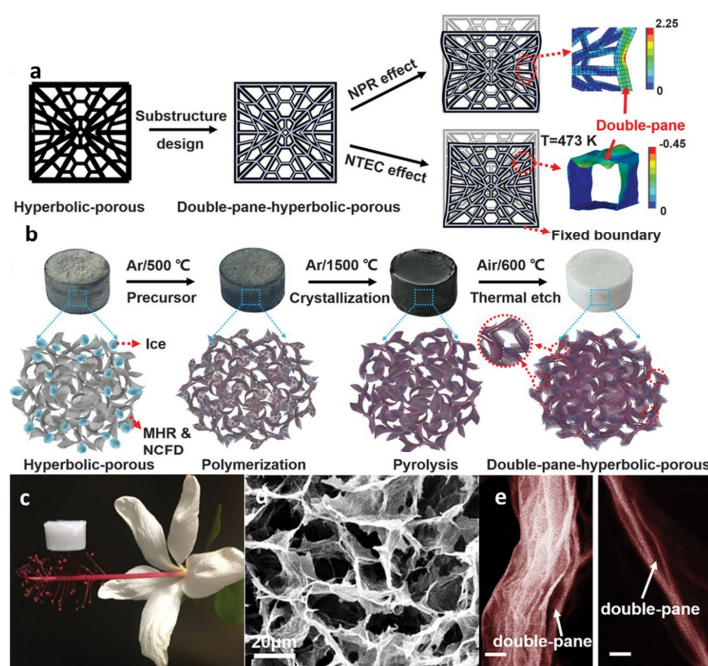
Figure 12. Structure design and fabrication of the ceramic aerogel metamaterial. (**a**) Illustration of the metastructure design of ceramic aerogels. The units of the colored scale bars are as follows: kilopascals for NPR and percentage (with strain zoomed by 30 times) for NTEC. (**b**) Illustration of the CVD synthesis process of the double-paned hyperbolic ceramicaerogels. (**c**) An optical image showing an h-BNAG sample resting on the stamen of a flower. (**d**) SEM image of h-BNAG. (**e**) SEM images of the double-pane wall structure of h-BNAGs. Scale bars, 20 nm. Adapted from [138] with permission, copyright the American Association for the Advancement of Science, 2019.

4. Applications

Combining the functionalities introduced by nanoscale materials with large surface area of aerogels opens many applications in environment remediation, energy storage, drug delivery and more.

4.1. Environmental Remediation

Porous Sorbents

The large surface area, high porosity, and light weight make aerogels promising sorbent materials. For example, aerogels have been used for environmental remediation to remove spilled oil, organic compounds and heavy metal ions [140]. The wetting properties of aerogels are important in achieving optimal adsorption performance. From this perspective, hydrophobic sorbent materials are of intense interest for application in absorbing hydrocarbons (Table 1). In one study, hydrophobic composite aerogels were fabricated from polysilsequioxane-containing phenylene and hexylene-bridge groups through the polymerization of the polysilsequioxane followed by supercritical drying [141]. The incorporation of the phenylene and hexylene-bridged groups increased the crosslinking density and the molecular weight of the composite aerogel, leading to a significant improvement in the mechanical properties of the aerogel. Additionally, a higher condensation rate of the hexylene-bridged groups produced a more hydrophobic aerogel (contact angle 115°) than the phenylene-bridges (92°). For example, a resorcinol-furfural/silicone hybrid aerogel was fabricated through a facile pressure-drying system at room temperature [142]. In this study, carbon nanotubes were used as a reinforcement material and a trimethylethoxysilane (TMES) solution was used as a surface modifier to increase the hydrophobicity of the aerogel. The TMES replaced the surface hydroxyl groups on the aerogel with stable $-OSi(CH_3)_3$ groups. By doing this, the contact angle increased from 108° to 135°. The highest contact angle was obtained when the ratio of TMES: hexane was 8:1. Another study proposed an interesting method to obtain hydrophobic aerogels through modifying silica gel networks with silylating agent dimethoxy-methyl (3,3,3-trifluoropropyl) silane [143]. The aerogels were synthesized from tetraethoxy silane (TEOS) using a two-step sol-gel process followed by a supercritical drying with CO_2. Duan et al. observed that adding silylating agent to the already produced TEOS gels achieved better results, with the contact angle increasing from 27.5 ± 0.3° to 142.2 ± 0.8°. The addition of the silylating agent significantly affected the resulting hydrophobicity. After the hydrolysis, the TEOS underwent rapid condensation, and gel formation occurs. If the TEOS and silylating agent molecules co-condensed, many of the hydrophobic groups were not exposed to the particle surface. Allowing the hydrolysis before the addition of silylating agent allowed for more functionalization of the gel network surface. The increase in the contact angle for the post-gelation samples was due to the silylating attachment mainly on the exterior of the gelled TEOS particles. In addition to these method studies, it was shown that by increasing wt.% of silylating agent from 5 to 25, contact angle could be increased from 70.6 ± 0.9° to 154.1 ± 0.5°.

Table 1. Comparison of hydrophobic composite aerogels.

| Materials	Contact Angle	Density (g cm^{-3})	Absorption Capacity	Compressibility	Ref.
Cellulose-based aerogel	140°	0.0196	35 (g/g)	80%	[144]
Polyvinylpolydimethylsiloxane-based aerogels	140–157°	0.02–0.2	1200–1600 (%)	-	[145]
Polymethylsilsesquioxane-silk fibroin aerogel	135° < θ < 145°	0.08–0.23	~500–2600 g g^{-1} %	80%	[146]
Clay composite aerogel with water repellent (WDisRep3)	140°	0.109	-	-	[147]
Magnetic hydrophobic polymer aerogel	138°	0.01384	59 to 136 times more than its original weight	-	[148]
Silica-silylated aerogel	154°	0.135	-	-	[143]
Silica-chitosan aerogel	137°	0.062	30 g/g	-	[149]
Magnetic polystyrene/ graphene aerogel	142°	0.005	40 times more than its mass	-	[150]
Natural Cellulose Aerogel (Cotton Source)	142°	-	100–140 g/g	-	[142]

A new rapid supercritical extraction process has been reported by Jung et al. to produce hydrophobic and transparent aerogels suitable for window shielding [151]. The hydrophobic character was introduced by adding poly(methylmethacrylate) to a silica gel, resulting in the addition of –OCH$_3$ and –CH$_3$ free radicals onto the surface. A silica solution formed the gel structure with the supply of inert gas pressure. Then it was promoted at supercritical conditions through continuous heating. As mentioned previously, cellulose has been used widely in aerogels; however, the hydrophilicity and inferior mechanical properties of cellulose aerogels limit their applications in absorbing organic contaminants. Yu et al. produced high-performance cellulose aerogels by freeze-casting aqueous suspensions of polyvinyl alcohol and cellulose nanofibrils in the presence of hydrolyzed methyltrimethoxysilane sol [152]. The silanol groups (Si–OH) reacted with hydroxyl groups on PVA and cellulose, as well as condensed among themselves to form a Si–O–Si network, leading to robust hydrophobic aerogels. The aerogel has a high absorption capacity of 45–99 times of their own weights, high oil/water selective sorption, and excellent reusability with absorption retention of more than 84% after 35 absorption–squeezing cycles (Figure 13).
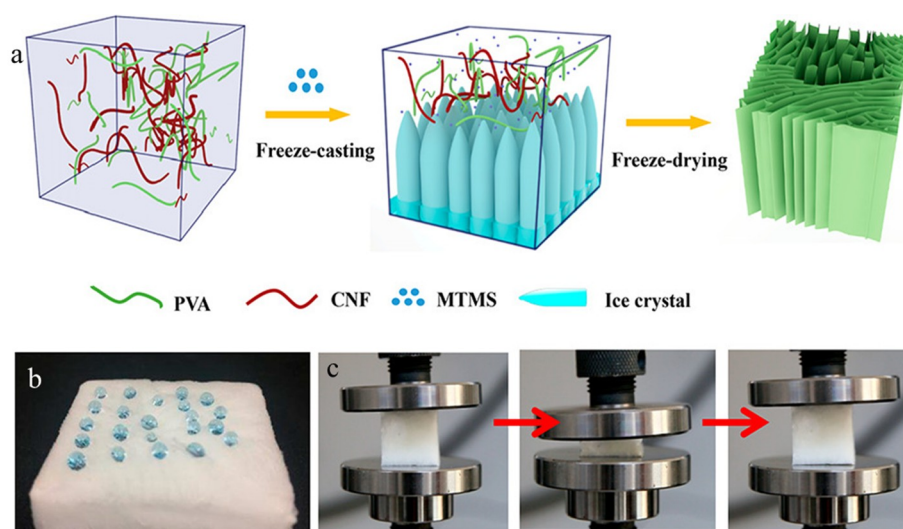
Figure 13. (**a**) A schematic illustration of fabricating hydrophobic cellulose aerogels. (**b**) A picture showing water droplets on the aerogels. (**c**) Pictures showing recovering of an aerogel from compression. Adapted from [152] with permission, copyright the American Chemical Society, 2019.

Commercially available, flexible and mechanically durable fiber-reinforced silica aerogel composites have been evaluated for oil spill cleanup (Figure 14) [153]. Thermal Wrap (TW) (6.0 mm thickness, Cabot Corporation, Boston, MA) is a composite of trimethylsilylated silica aerogel particles attached on bicomponent polyester fibers, and Spaceloft (SL) (10 mm thickness, Aspen Aerogels, Northborough, MA, USA) is a composite of a lofty fibrous batting of polyester and glass fibers infiltrated with trimethylsilylated silica aerogel and magnesium hydroxide. As shown in Figure 14, both aerogel blankets have hydrophobic silica nanoparticles attaching to fibers, leading to a hydrophobic/oleophilic property. The study indicated that these aerogel composites possessed three important desirable properties for oil spill cleanup: fast oil sorption (3–5 min), reusability (demonstrated over 10 cycles with preserved tensile strength for TW; 380–700 kPa), and recoverability (up to 60% via mechanical extraction).
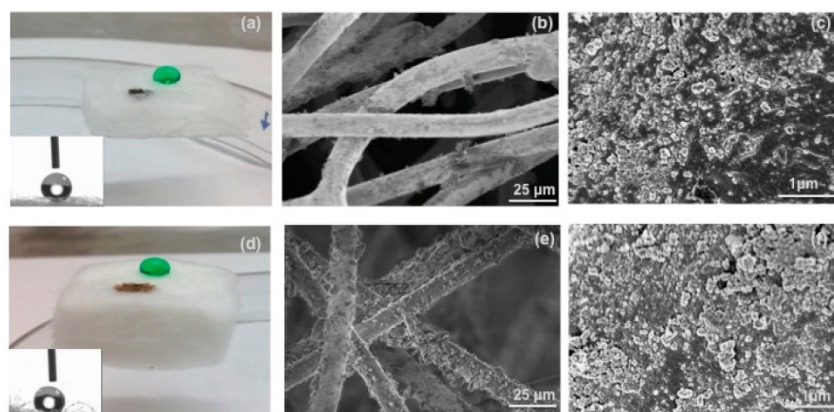
Figure 14. Optical interrogation of aerogel fabrics' gross and fine structure. Image of a dyed-green water droplet and Iraq oil on the surface of (**a**) TW (6 mm thick) and (**d**) SL (10 mm thick). Insets are images from the WCA measurements. Please note that the TW used is thinner than SL. SEM images of the surfaces of (**b** and **c**) TW and (**e** and **f**) SL, where aerogel particles are visible on the fibers in high-resolution. Reprinted from [153] with permission, copyright American Chemical Society, 2016.

4.2. Energy Storage

Over the past decades, great research efforts have been devoted to building high-performance, cost-effective, renewable, and sustainable energy storage devices to meet the need for renewable energy, electric vehicles, and portable electronics. Among many devices developed to address such needs, advanced batteries and supercapacitors are leading this quest. Batteries, owing to their high energy density and ability to supply a constant source of electrical power, dominate the worlds of portable electronics and electric vehicles. This is especially true for lithium-ion type batteries (LIBs) [154]. Supercapacitors, on the other hand, are ideal for short-term energy needs due to their extremely quick and high efficiency charging capabilities, while also being able to operate for a virtually unlimited number of charge-discharge cycles [155,156]. Thus, batteries and supercapacitors are complementary energy storage devices [157].

Improving battery and supercapacitor electrodes is essential to offer higher capacitances and efficiencies, lower the costs, and create more eco-friendly devices. Carbon aerogels have been at the forefront of such research efforts due to carbon's inherently high surface area, chemical stability, low cost, and eco-friendliness [158]. The hierarchical porous carbon framework in aerogels greatly increases the ability to store electric charge by enabling faster electrolyte ion diffusion rates, creating more active sites for the energy conversion process, and presenting a continuous charge transfer pathway [159]. For batteries, the aerogel structures create space within the electrode to accommodate any volume changes that occur during the charge–discharge cycles that is unavailable in traditional electrode materials [160].

The chemistry, fabrication, and properties of a variety of carbon-based aerogels have been extensively studied for energy storage applications [161–163]. While carbon nanotubes, graphene, and graphene derivatives have been used extensively in producing aerogels for energy storage applications [119], bio-based carbon materials are abundant and extremely cost-effective, while offering biodegradability and biocompatibility [164,165], offering flexible, fully disposable electrodes [156,166]. This section aims to provide an overview of the electrochemical performances of graphene and cellulose-based aerogels as LIB and supercapacitor electrodes over the last few years.

4.2.1. Supercapacitors

Graphene aerogels have often been composited with conductive polymers and highly electroactive nanoparticles in order to create supercapacitor electrodes with very high capacitances and cycling stabilities. Graphene functions as a support of polymers and nanoparticles with larger surface

area and electrical conductivity. Many unique strategies have been employed to offer fabrication techniques that are both affordable, eco-friendly, and easily scalable. Zhai and coworkers fabricated high-performance supercapacitor electrodes using graphene aerogel (GA) doped with palladium (Pd) nanoparticles (Figure 15a) [167]. The SEM images of GA and P-GA samples and the TEM image of Pd nanoparticles showed that Pd nanoparticles uniformly distributed on graphene surfaces (Figure 15b–d). Pd nanoparticles caused a significant reduction of the electrical resistivity by 50 times (i.e., from 950 to 16 Ω cm) compared with pure GAs. Additionally, a negative electrode based on P-GA showed a specific capacitance of 175.8 F/g at a scan rate of 5 mV/s, which is more than 3 times enhancement as compared to that without Pd doping (51.9 F/g). The MnO_2//P-GA asymmetrical supercapacitors were produced from the composite aerogel electrodes and demonstrated an average energy density of ≈13.9 Wh/kg at a power density of ≈13.3 kW/kg, which was much higher than other graphene- and carbon-based asymmetrical supercapacitors. (Figure 15e,f). Reduced graphene oxide (rGO) and polypyrrole (PPy) composite aerogels were produced by Sun and co-workers employing a spontaneous self-assembly approach [168]. In their study, pyrrole was added to an aqueous graphene oxide (GO) suspension, where pyrrole was polymerized and deposited on reduced GO to obtain the rGO-PPy hybrid hydrogel. The hydrogels were washed with ethanol and supercritically dried with CO_2. Through combining the GO sheets with the PPy, aggregation of the GO sheets was prevented, which created a thin walled, hierarchical porous structure of the hybrid aerogels. The CV curves of such aerogels indicated both pseudocapacitive and electrochemical double layer capacitance (EDLC) with a specific capacitance of 304 F/g at a current density of 0.5 A/g (Table 2). While showcasing the promise of such a one-step fabrication method for graphene aerogel hybrids, these materials quickly degraded performing at only 58% of their original capacitance after 50 cycles.
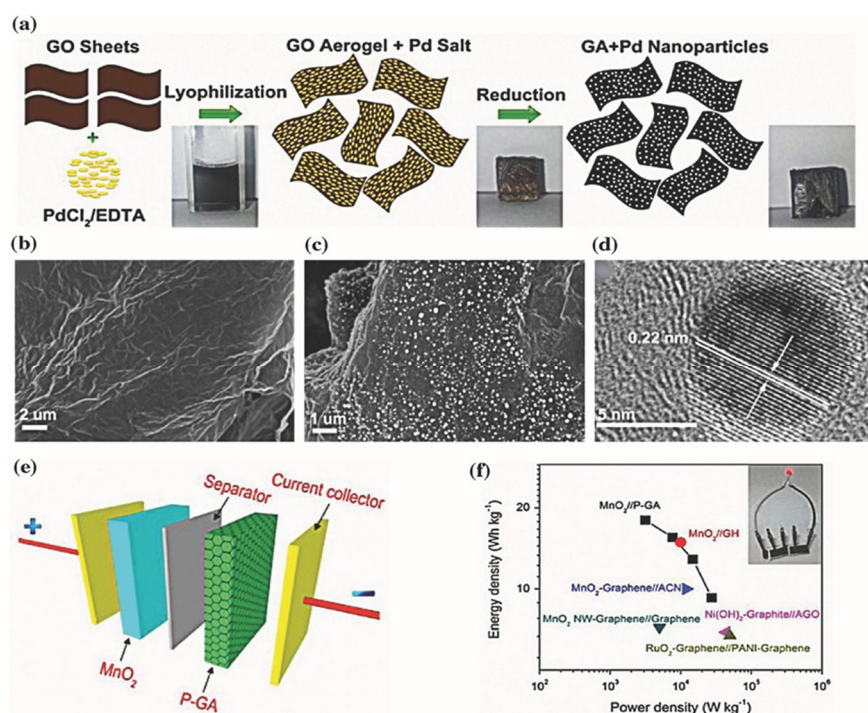
Figure 15. (**a**) Schematic illustration showing the fabrication process of P-GA. (**b**,**c**) SEM images of the GA (**b**) and P-GA (**c**). (**d**) HRTEM images of P-GA. (**e**) Schematic showing ASC device construction using MnO_2 and P-GA electrodes. (**f**) Ragone plot reflecting the superiority of P-GA nanostructures over other electrode materials. The inset shows a red LED powered by using two devices connected in series. Reprinted from [167] with permission, copyright American Chemical Society, 2015.

Other researchers have utilized another conducting polymer polyaniline (PANI) to create hybrid graphene aerogel supercapacitor electrodes. For example, Yang et al. produced a GO aerogel through a hydrothermal treatment (180 °C, 1 h) and freeze-drying of an aqueous suspension of PANI nanowires and GO [158]. The PANI nanowires in the suspension interacted with the basal planes of the GO, preventing GO from aggregating and providing fast ionic channels within the electrode materials. These composite aerogel electrodes had a capacitance of 520 F/g at a current density of 0.25 A/g with a retention of 89% after 500 charge-discharge cycles. Furthermore, highly electrochemically active cobalt salt nanoparticles (3560 F/g theoretical capacitance) have been added to PANI/GO aerogels via a hydrothermal treatment (180 °C, 6 h) and freeze-drying [169]. The synergy of the GO sheets and Co_3O_4 and PANI nanoparticles led to a capacitance of 1247 F/g at a current density of 1 A/g with minimal degradation after 3500 charge-discharge cycles.

Carbon nanotubes (CNTs) are generally used in graphene aerogels to space the GO sheets and prevent graphene from aggregating to increase the hierarchical porosity and available actives sites for energy storage and electrolyte ion transfer. For example, singled-walled CNTs (SWCNTs) were dispersed with GO followed by a hydrothermal treatment (180 °C, 12 h) and freeze-drying [170]. It was demonstrated that SWCNT/GO composite aerogels provided three-dimensional (3D) macro-porous structures to improve the accessibility of electrolytes, and conductive SWCNTs reduced the electrical resistance. The composite electrodes have a capacitance of 246 F/g at 2.5 A/g current density, with outstanding high stability, retaining 97% of original capacitance after 2000 cycles. While most often used as a spacer, several studies have shown that CNTs can indeed provide the aerogel base for supercapacitor electrode production. In one such study, CNTs were coated with nitrogen-doped graphene in order to create a highly flexible, wire-like electrode [171]. In one of the most unique processing strategies found in the literature, these aerogel electrodes were fabricated by forming CNT hydrogel on the tips of carbon nanofibers (CNF), followed by dipping the hydrogel in a dopamine solution. The dopamine was then crosslinked and pyrolyzed at 800 °C in order to create the N-doped graphene-coated CNT aerogels. These CNT aerogel electrodes were highly flexible, maintaining 91% of their original capacitance after being stretched and released for 10,000 cycles, something not often seen in carbon aerogel electrodes unless cellulose nanomaterials are used to create the aerogel.

Table 2. Comparison of the capacitance and stability of select graphene, carbon nanotube, and cellulose aerogel composites for supercapacitor electrodes. * Areal capacitances reported only. ** Values not reported for this paper.

Carbon Precursor	Modification	Capacitance [F/g]	Stability	Test Conditions	Electrolyte	Ref
Graphene Oxide	Polypyrrole	304	58%, 50 cycles	0.5 A/g, 3-electrode	6 M KOH	[168]
Graphene Oxide	PANI Nanowires	520	89%, 500 cycles	0.25 A/g, 3-electrode	1 M H_2SO_4	[158]
Graphene Oxide	Polyvinyl alcohol	295	85%, 2000 cycles	1 A/g, 3-electrode	1 M H_2SO_4	[119]
Graphene Oxide	PANI/Co_3O_4 NP	1247	Minimal decrease	1 A/g, 3-electrode	6 M KOH	[169]
Graphene Oxide	PANI Crosslinker	480	96.1%	1 A/g, 3-electrode	1 M H_2SO_4	[172]
Graphene Oxide	PANI-*g*-rGO	1680	91%, 3000 cycles	1 A/g, 3-electrode	6 M KOH	[159]
Graphene Oxide	SWCNT	246	97%, 2000 cycles	2.5 A/g, 3-electrode	5 M KOH	[170]
Microcrystalline Cellulose	Co_2 Activation	302	92%, 4000 cycles	0.5 A/g, 3-electrode	6 M KOH	[89]
Cellulose (Bamboo)	KOH Activation	215	Not Reported **	0.2 A/g, 3-electrode	6 M KOH	[166]
CNF (Kraft Softwood)	Ag/PANI NPs	176 mF/cm² *	Not Reported **	10 mV s^{-1}, 2-electrode	1 M H_2SO_4	[156]
CNC (Cotton)	PPy-NF	1.5	84%, 2000 cycles	0.2 mA/cm², 3-electrode	Na_2SO_4	[165]
CNC (Cotton)	PPy-Coated CNT	1.3	62%, 2000 cycles	0.2 mA/cm², 3-electrode	Na_2SO_4	[165]
CNC (Cotton)	MnO_2-NP	1.1	92%, 2000 cycles	0.2 mA/cm², 3-electrode	Na_2SO_4	[165]
CNF (Kraft Softwood)	PPy coating	215	97–111%, 2000 cycles	0.19 mA/cm², 2-electrode	LiCl-PVA	[173]

Carbon aerogels based on biological carbon can come from many cost-efficient and eco-friendly sources, such as grasses, trees, and sea tunicates, which provide excellent sources of cellulose nanocrystals and nanofibers. Flexible all solid state supercapacitor (ASSS) electrodes have been fabricated from CNF isolated from kraft softwood [156]. The CNFs were coated with silver (Ag) nanoparticles followed by PANI through electrodeposition. The unique nanostructure consisted of a continuous cellulose network coated by a grape-like structure of 10–100 nm Ag particles which was covered in PANI nanodots. These electrodes had a capacitance of 215 F/g at a current density of 0.2 A/g, and were able to be maintained, even in a bent state, which paves the way for flexible electronics. Cellulose nanocrystals (CNCs) have been isolated from Whatman cotton filters and bonded with more electroactive nanomaterials such as PPy, CNTs, and MnO_2 nanoparticles to produce supercapacitor electrodes [165]. In this study, three types of aerogel electrodes were produced by dispersing the isolated CNCs with PPy-coated CNTs, PPy nanofibers, and MnO_2-nanoparticles in water prior to creating the dry aerogel through freeze-drying. Of the three hybrid CNC electrodes, the MnO_2 nanoparticle modified aerogel had the lowest specific capacitance, but the highest retention of the capacitance after 2000 cycles. On the other hand, the PPy nanofiber-modified CNC aerogels possessed the highest capacitance with decent cycle stability. The CNC-based electrodes are very flexible and are able to recover up to 90% of their original shape after being mechanically deformed.

Adding three-dimensionality to supercapacitors can boost the areal energy density to allow for practical applications in high-energy systems. However, there is typically a trade-off limitation of increasing the mass loading with ionic transport resistance. Thus, 3D supercapacitor electrode architecture needs to be engineered in a way to obtain super-elastic 3D electrodes with increased mass loading, apparent density, and thickness without decreasing electron and ion transport rates. A graphene ink was developed to retain its shape after being deposited via DIW 3DP [174]. The optimal rheological behavior of the ink was obtained by adding hydroxyproplmethylcellulose as a viscosifier, along with an amphiphilic triblock copolymer pluronic F127 (poly(ethylene oxide) (PEO)-poly(propylene oxide) (PPO)-PEO) as a gelling agent to induce viscoelastic properties and a template to generate mesopores. The complete processing schematic is provided in Figure 16. The structural integrity of the 3D-printed graphene was retained during drying and carbonization for a successful conversion into a compressible cubic lattice graphene aerogel (GA). Upon printing of the cubic lattices, the aerogels demonstrated excellent structural integrity and microarchitectural accuracy, indicating high quality printing. Polypyrrole (PPy) was also chemically deposited on the graphene aerogel scaffolds to increase the specific capacitance, from 14 to 393 F/g, and enhance certain mechanical properties such as compressive strength from 0.14 to 2.4 MPa. The composite PPy-GA electrode had capacitance and energy density of 2 F/cm^2 and 0.78 mWh/cm^2, respectively.

4.2.2. Lithium-Ion Batteries

Graphene and its derivatives have been extensively investigated for lithium-ion battery (LIB) electrodes, where they are mixed with electroactive species, such as TiO_2 and MoS_2, without the use of other binders or conductive agents. For example, Jiang and coworkers combined GO and MoS_2 by a one-pot, hydrothermal treatment (180 °C, 24 h) [155]. The hybrid hydrogels were reduced with hydrazine hydrate followed by freeze-drying to produce a hybrid aerogel. The interactions between GO and MoS_2 nanosheets granted a high storage capacity of 1200 mAh/g and high cycling stability, retaining 95% of their original capacitance after 200 cycles. This system had a substantially higher lithium storage capacity than pure graphene (372 mAh/g) or MoS_2 (670 mAh/g), indicating the highly synergistic nature of this system. He and coworkers created a sandwich structure between graphene and MoS_2 which further enhanced the storage capability and stability of the electrode [175]. In this study, graphene-MoS_2 aerogel anodes were fabricated via a similar hydrothermal (260 °C, 36 h) and freeze-drying treatment where alternating ultrathin layers of graphene oxide and MoS_2 provided efficient electron transfer and short lithium ion diffusion channels. This led to a storage capability of 1298 mAh/g at 0.1 A/g, retaining 99% of this capacity after 200 cycles. In some other studies,

polymers were used to increase the interaction between the electroactive species and the graphene oxide. For example, the hydroxyl groups of glucose were used to covalently link titanium dioxide (TiO_2) nanoparticles with the (001) face of graphene [176]. The obtained composite anode had a high storage capability of 605 mAh/g and demonstrated high compression flexibility attributed to the glucose linkers. Although the anode had low cycling stability, maintaining only 33% of its original capacity after 50 cycles, it could be used in the design of next generation flexible battery.
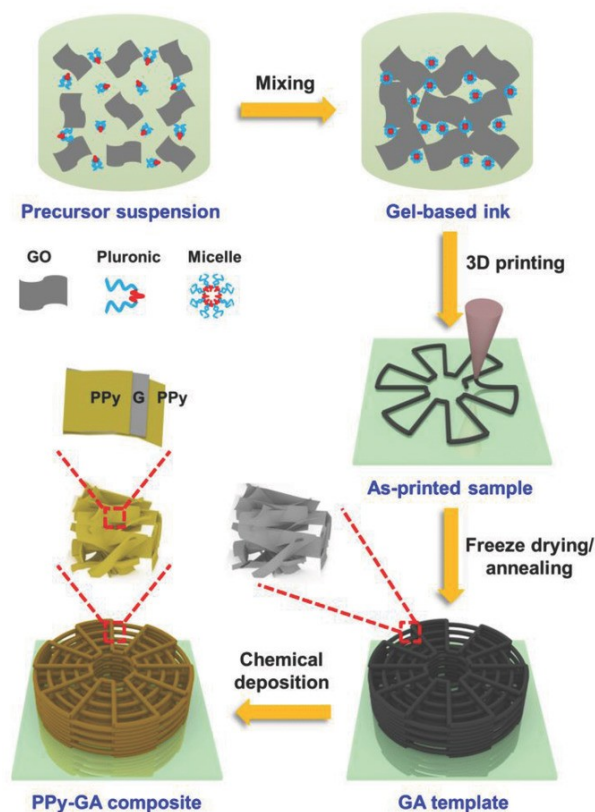
Figure 16. Schematic of the processing of 3D-printed graphene-based composites for supercapacitors. Reproduced from [174] with permission, copyright John Wiley & Sons, 2018.

Cellulose-based carbon aerogels have been used as anodes and polyelectrolyte separators in LIBs. Cellulose aerogels, as anode materials, often serve as supports for electroactive nanoparticles such as iron oxides. For example, flexible and binder-free LIB anodes were fabricated through decorating bacterial cellulose nanofiber aerogels with nanoparticles of Fe_3O_4 [177]. These electrodes were made through hydrothermal treatment (120 °C, 10 h) of bacterial cellulose pellicles in a 0.05 M $Fe(NO_3)_3 \cdot 9H_2O$ solution. The sol-gel was then freeze-dried and carbonized. Fe_3O_4 nanoparticles evenly attached on the CNF surfaces through the interaction with –OH groups on cellulose. The electrical conductivity of these samples was determined to be 2.0 S/m and 2.1 S/m before and after repeated bending, respectively, showing the flexibility of such anodes. Starting with a very high storage capacity of approximately 1000 mAh/g, these electrodes showed decent stability during the charging–discharging cycles, retaining about 75% of their original capacity after 100 cycles. Fe_2O_3 nanoshells were deposited onto the surface of carbon nanofiber aerogels produced through pyrolysis of cellulose aerogels [178]. In this work, carbon fiber aerogel was impregnated with Fe_2O_3 via an immersion in a $Fe(NO_3)_3 \cdot H_2O$ solution followed by drying and subsequent heat treatment at 200 °C for 10 h in air. The resulting amorphous network was highly flexible and presented a high capacity of 1195 mAh/g when analyzed as an anode in a 1 M$LiPF_6$ electrolyte (1:1 EC/DMC). The highly interconnected network of carbon and Fe_2O_3 nanoshells yielded this improvement in capacity while the highly porous, flexible nature of the aerogel

mitigated the issues with large volume changes at higher current densities, enabling such an electrode to still possess a high capacitance of 1115 mAh/g at 0.8 A/g.

Cellulose aerogels have significantly improved ionic conductivity and wettability demonstrated as polymer electrolyte separators due to the porous and hydrophilic nature of the cellulose. For example, Liao and co-workers fabricated a polymer separator by coating hydroxyethylcellulose aerogels onto a polypropylene (PP) film [179]. The composite film had a superior thermal stability, good ionic conductivity, and higher electrolyte uptake and retention when compared with traditional polymer electrodes. Cellulose aerogels were also used as the polymer electrolyte for LIBs [180]. In this work, a cellulose aerogel membrane was developed through a typical sol-gel method with an ionic liquid prior to supercritically drying in CO_2. This aerogel separator exhibited improved ionic conductivity and electrolyte uptake and retention and had negligible capacity loss after 100 cycles. Compared to LIB cells utilizing a standard electrolyte separator, LIBs with cellulose aerogels showed an improvement in the specific rate capacity from below 70 mAh/g to 80.5 mAh/g.

CNTs have been used in the forms of foams, mats, arrays, and encapsulating devices for applications regarding lithium-sulfur, lithium-telluride, and sodium-ion battery electrodes [181–188]. CNT aerogels have been combined with a covalent organic framework (COF) for the application as LIB electrodes [189]. COF with a redox-active naphthalene diimide wall was grown on the conductive CNTs to introduce synergistic electrochemical properties to the aerogel. The COF, being insoluble, helps to create a robust electrode while the interconnected network of CNTs helps to facilitate charge transfer and electrolyte diffusion. Although the CNT aerogel had a unique structure, it possessed a meager capacity compared to all other aerogels, as can be seen in Table 3. It is apparent that in order to employ CNTs as aerogels for battery applications, more innovative and unique approaches must be considered in order to increase the capacity while forming a stable and reliable electrode material.

Table 3. Comparison of select carbon aerogel electrodes for lithium-ion batteries.

Carbon Precursor	Modification	Anode/Cathode	Capacity [mA h/g]	Stability	Testing Conditions	Electrolyte	Ref.
Graphene Oxide	TiO_2/glucose	Anode	605	33%, 50 cycles	0.1 A/g	1 M LiPF6, EC/DMC	[176]
Graphene Oxide	MoS_2	Anode	1200	95%, 200 cycles	0.1 A/g	1 M, LiPF$_6$,EC/DMC	[155]
Graphene Oxide	MoS_2	Anode	1298	99%, 200 cycles	0.1 A/g, 2-electrode	1 M LiPF$_6$, EF/DMC	[175]
Graphene Oxide	PAQS	Cathode	156	71%, 1000 cycles	0.1 C, 3-electrode	0.1 M NaPF$_6$,DME/DOL	[154]
CNT	COF	Cathode	67	Not reported *	0.5 mV/s	1 M LiPF$_6$, EC/DMC	[189]
Cellulose (Bacterial)	Fe_3O_4	Anode	1000	75%, 100 cycles	0.1 A/g, 2-electrode	1 M LiPF$_6$ in EC/DMC/EMC	[177]
Cellulose (Bacterial)	Fe_2O_3	Anode	1195	Not reported *	2-electrode	1 M LiPF$_6$, EC/DMC	[178]

4.3. Biomedical Applications

The typical low density, high porosity, and high surface area of aerogels make them suitable for many biomedical applications, including drug delivery, tissue engineering, implantable devices, biomedical imaging, and biosensing [190–193]. Previously, only silica-based aerogels had been investigated for the use in these applications; however, their poor biodegradability inhibited their use in pharmaceutical and biomedical applications [194,195]. At present, polysaccharides such as starch, alginate, and chitosan are being investigated as biomedical aerogels as they provide low toxicity, biocompatibility, and biodegradability [190]. The following sections will briefly review some of the current and potential biomedical applications for such polymer and polymer-composite aerogels.

4.3.1. Drug Delivery

Treatments for diseases such as cancer utilize toxic agents that can unintentionally harm the patient/subject/host. To mitigate such issues, delivery systems have been considered to encapsulate drugs to reduce the negative effect. The use of a drug delivery system enables a higher efficiency, better protection from degradation, and targeted release of the drug [196,197]. By encapsulating the drug within a delivery system, surface modification can be achieved to allow for specific targeting [197]. With high porosity, low density, and biocompatibility, aerogels have been at the forefront of novel drug delivery system development [196]. The high porosity of the aerogel enables a significantly higher loading capacity of the drug while the supercritical drying step of typical aerogel fabrication processes facilitate the impregnation of the drug without the use of organic solvents and high temperatures [190, 194] Previously, synthetic polymers such as polyethylene, polypropylene, and polydimethylsiloxane have been used for drug delivery systems; however, non-biocompatibility of these polymers is problematic. To resolve this issue, polysaccharides and their derivatives serve as a better template because of their biocompatibility, stability, availability, and renewability [198].

The use of polysaccharides such as chitosan, alginate, and starch have been the focus in natural polymers for many biomedical applications and extends in the realm of biomedical aerogels. However, little has been reported with regard to the polysaccharide, glucan. Salgado et al. studied the formation of a barley and yeast β-glucan aerogel for the oral delivery of acetylsalicylic acid [190]. β-glucan can help wound healing with an antimicrobial and anti-inflammatory nature. Barley β-glucan lowers blood cholesterol and reduces the likelihood of heart disease. The β-glucan aerogels were fabricated by aqueous gelation, solvent exchange, and supercritical drying in CO_2. Barley β-glucan (BBG) hydrogels created more sponge-like structure, whereas yeast β-glucan (YBG) produced a more crosslinked configuration that demonstrated improved water uptake. The acetylsalicylic acid was loaded into the β-glucan aerogels by impregnation via supercritical drying. In the in-vitro release study, the BBG aerogels revealed a time lag (i.e., negligible release) of up to 3 h and a fast release of 60% from 3 to 8 h. YBG aerogels demonstrated an initial quick release during the first 2 h while keeping the drug release sustained for the 24-h study. The two systems demonstrated different release mechanisms based on the capacity to uptake water.

It was previously mentioned that silica derived aerogels are not biodegradable. However, the use of silica in biomedical aerogels is still present, as they are biocompatible, and possess a high surface area and an open pore structure. Although polysaccharides bypass the complications of silica, they have a lower surface area and release efficiency (e.g., Ca-alginate). Silica/alginate hybrid aerogels can combine the properties of silica and the biodegradability and bioadhesive characteristics of alginate. A silica/alginate hybrid aerogel was fabricated and loaded with ketoprofen, a poorly water-soluble non-steroidal anti-inflammatory drug. The hybrid aerogels were produced by using an emulsification/internal setting technique in which a water phase containing silica and alginate were introduced to an oil phase, creating a water-in-oil emulsion. The solution was mixed until a hybrid hydrogel was formed, following phase inversion to separate the hydrogel in the water phase. The hydrogels underwent a series of solvent exchanges with varying concentrations of ethanol forming alcogels. Alcogels were then immersed in a solution of ketoprofen and supercritically dried with CO_2 at 40 °C. In the hydrogel or alcogel phase, the particles were coated with three different solutions of Ca-alginate/hydoxypropyl methylcellulose (HPMC), silica/HPMC, and a hydrophobic silica. Results revealed that the surface area of the hybrid aerogel particle was over 900 m^2/g, compared to alginate particles with a specific surface area of 680 m^2/g. Drug release studies revealed that uncoated aerogels could serve potential in burst release as 90% of the drug was released in 3 min compared to free drug release of 240 min. Coated aerogels demonstrated higher loading of drug with the 104 mg/g for Ca-alginate/HPMC-coated aerogels compared to 24 mg/g for uncoated aerogels [199].

Synthetic and naturally derived polymeric aerogels have also been investigated for use in drug delivery applications. For example, a thermo/pH responsive aerogel was fabricated for the controlled release of indomethacin, a hydrophobic drug model [194]. Alginate was grafted with

N-isopropylacrylamide and *N*-hydroxymethylacrylamide via radical polymerization. The resulting hydrogel was washed with deionized water and freeze-dried in order to form the aerogel. By adjusting the ratio of co-polymers grafted onto the alginate backbone, the thermo-responsive behavior could be tuned while simultaneously altering the lower critical solution temperature (LCST). The drug-loaded aerogel was released at various pH and temperature levels. Here, pH (2.1 and 7.4) and temperature (25 °C and 42 °C) were investigated. It was found that above the LCST (37.8 °C), the polymer chains would aggregate and shrink resulting in higher release of the indomethacin when compared to below the LCST. At neutral pH, the indomethacin was completely released while only 10% released under acidic conditions. This dual responsive release showed excellent potential in biomedical applications for controlled release systems as the aerogel must overcome both boundaries to release the drug, allowing for a more sensitive and controlled release.

3D-printed aerogels have been produced for drug delivery applications. For example, thermal inkjet printing (IJP) was used to build alginate aerogel particles impregnated with salbutamol sulfate (SS), a drug used to treat asthma and chronic obstructive pulmonary disease [200]. Thermal IJP is a promising method that allows the processing of printed particles for drug delivery systems with reproducible, narrow particle size distribution and high spatial resolution. In this method, the alginate aerogel particles were printed via a "drop-on-demand" mode followed by supercritical drying, resulting in the formation of monodispersed nanoparticles with a unique nanostructure displayed in Figure 17. Gel beads formed once the alginate solution made contact with the CaCl$_2$ gelation bath. The gel beads were then left for 5 h for aging and then subjected to either a direct (×2) or sequential (ethanol:water volume ratio 0:100, 50:50, 75:25, 100:0 (×2)) solvent exchange to ethanol. The direct exchange (Figure 17A) resulted in an optimized solvent method as there was no loss in particle sphericity nor appearance of dimples, as observed for the serial exchange method. In vitro release of the SS in PBS demonstrated that 10% of the total drug was released during the first 10–15 min. After the initial burst, a sustained release of the remaining drug occurred for 10 h. This unique IJP processing of alginate particles shows great promise to reduce drug administration frequency when compared to traditional powder inhalers that must be re-administered every 4–6 h.
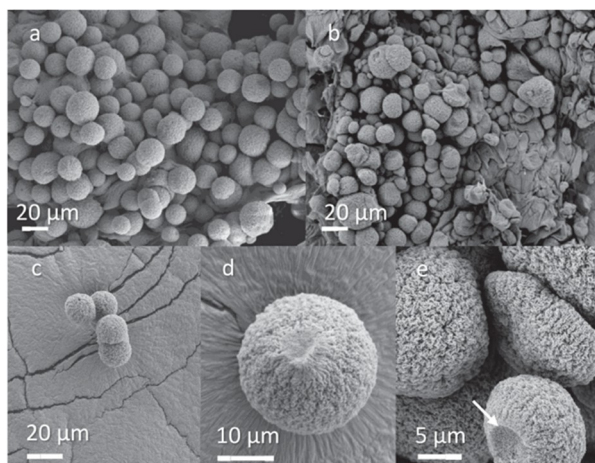
Figure 17. Scanning electron microscopy (SEM) images of microgel particles printed via IJP of aqueous alginate solutions into baths of CaCl$_2$ with (**a**,**c**–**e**) direct or (**b**) sequential solvent exchange. Reproduced from [200] with permission, copyright Elsevier B.V., 2018.

4.3.2. Tissue Engineering: Scaffolds

Over the last few decades, tissue engineering has focused on the regeneration, reconstruction or replacement of damaged tissues. Characteristics such as cell growth, attachment, differentiation, proliferation, and tissue vascularization are needed for tissue engineering scaffold [191]. In the past, traditional sources for tissue engineering material originated from harvesting tissues from

both humans and animals. However, lack of donors, negative immune response and infection are problems that can occur [88]. To overcome these issues, polymer-based aerogels serve as potential 3-dimensional (3D) scaffolds for tissue engineering, as they have demonstrated the capability of supporting such cellular activities [88]. Biocompatibility and biodegradability are also sought after for scaffold development. For these reasons, natural and synthetic polymers such as collagen, gelatin, alginate, chitosan, hyaluronic acid, and silk fibroin are of intense interest for the development of aerogels for such scaffolding applications [191].

One example of developing such aerogels for tissue scaffolds is an alginate-lignin hybrid aerogel with both micro- and macro-porosity [201]. Such a structure was achieved through CO_2 gelation and hydrogel foaming, followed by solvent exchange and supercritical drying. The combination of alginate and lignin allows for better cell adhesion, growth, and differentiation as the lignin decreases the hydrophilicity and increases the stability over pure alginate. Cell toxicity studies on mouse fibroblast cell line L929 demonstrated no cytotoxicity from the aerogels. Cell adhesion studies demonstrated that cells were able to attach to the aerogel and their metabolic properties increased from day 3 to 7, indicating a high potential of such an aerogel to be used for scaffolds in tissue engineering. In another study, a silk fibroin (SF) aerogel was investigated for its use as a tissue engineering scaffold [191]. In this work, the aerogels were synthesized via sol-gel fabrication, salt leaching, solvent exchange, and supercritical CO_2 drying, which resulted in a bi-modal pore distribution. When comparing SF aerogels fabricated by freeze-drying versus supercritical drying, it was found that different porosities were achieved where the supercritical drying yielded an aerogel with more surface area and a higher pore volume. Cytocompatibility between human foreskin fibroblast (HFF) and the SF aerogel was explored. It was determined that the aerogel was biocompatible, as uniform distributions of cells were found throughout the scaffold. Additionally, cell attachment and penetration studies revealed that a microporous scaffold was needed for cell viability and attachment.

Hybrid nanofiber aerogels were investigated for cranial bone regeneration in another study [192]. The hybrid nanofiber aerogel was composed of electrospun poly(lactic-*co*-glycolic) acid-collagen-gelatin (PLGA-PCG) nanofibers and strontium-copper co-doped bioglass (Sr-Cu-BG) nanofibers (Figure 18). The nanofibers were then sonicated in deionized water separately before being sonicated together to form an aqueous dispersion of PLGA-PCG and Sr-Cu-BG nanofibers. This hybrid dispersion was then freeze-dried and thermally treated with absolute ethanol to allow physical fusion of the overlapping nanofibers to create the resulting hybrid aerogel. The resulting aerogel was introduced to a solution of E7-BMP-2, a biomolecule that stimulates angiogenesis and osteogenesis, to allow loading. The loaded aerogels were then implanted into a defective region of the cranial bone of rats. The healing of the cranial bone was monitored via microcomputed tomography in order to visualize the healing at 4 and 8 weeks after implantation. The results show that after only 8 weeks, there was 65% closure of the defect bone and 68% coverage of the defect area. This study successfully presents a potential bone regeneration with this aerogel.

In a work by Maleki et al., silk fibroin (SF) was added as a biopolymer to improve the compressive strength and flexibility of pristine silica aerogels [146]. SF polymer/silica hybrid structures were synthesized by a one-step/ one-pot acid catalyzed sol-gel approach. This was done by preparing a solution of organosilanes, containing 5-(trimethoxysilyl)pentanoic acid (TMSPA) and tetramethylorthosilicate (TMOS), and an SF biopolymer in an aqueous acetic acid solvent in the presence of hexadecyltrimethylammonium bromide (CTAB). TMPSA was to form a stable covalent linkage between silica and the secondary silk fibroin structure and CTAB was used as a phase separation suppressing agent. The as prepared gel, with the optimal ratio of SF/silica mass fraction of 15:100 with the name ET-SF-15, was used to construct 3D structures via DIW printing because of its optimized viscosity. The as printed construct was then transferred to the oven for continuing the remaining gelation and aging steps, which was then solvent exchanged and dried supercritically. Upon studying the microstructure of the 3D-printed structure, no significant visible structural changes in the network were present as compared to the cylindrical monolith (not 3D-printed). This study demonstrated the

ability of DIW to tailor the micro- and macrostructure of the silica-SF aerogel hybrid, paving the way for such scaffold designs to be suitable for tissue engineering studies and regenerative medicine. Another study of nanocellulose demonstrated the 3DP of cellulose nanocrystal aerogels via DIW with well controlled structures and dual porous structures. It was concluded that these aerogels demonstrated the potential for different tissue engineering applications due to the ability of structural and inner pore architecture customization with this technique [202]. Thus, 3DP of aerogels presents a novel approach for creating customizable and complex architectures required for structures such as scaffolds for tissue engineering.
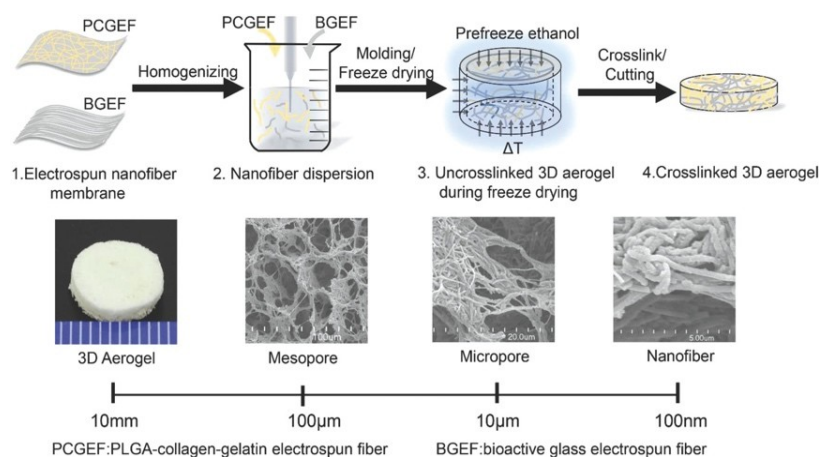

Figure 18. Schematic illustration of the fabrication of 3D hybrid aerogels from polymer nanofibers and bioglass nanofibers. Reprinted from [192] with permission, copyright John Wiley & Sons, 2018.

4.3.3. Tissue Engineering: Wound Healing

The normal wound healing process undergoes four phases: hemostasis, inflammation, proliferation, and remodeling [203]. Chronic wounds are the result of hypoxia, pH changes, and bacteria [204]. This results in abnormal healing, where the wound is stationary or prolonged in the inflammation phase and thus inhibits the normal healing process [204]. To promote healing, optimal oxygen permeability, normal cellular function, moisture control, and angiogenic conditions are needed [203,204]. The high porosity and surface area of aerogels create a potential for the material to be useful in wound healing treatments [204].

Nano-fibrillated cellulose (NFC) and copper containing mesoporous bioactive glass (Cu-MBG) aerogel composites were investigated for their potential treatment of chronic wounds [203]. These aerogels were fabricated by the introduction of Cu-MBG powder into a solution containing NFC in deionized water and mixed under stirring. The solution containing both the Cu-MBG powder and the NFC was filtered and dried in a vacuum desiccator at 40 °C. The purified compound was re-suspended in deionized water to form hydrogels, underwent solvent-exchange with organic solvents, followed by freeze-drying into the aerogel structure. The composite aerogels were cultured in a 3T3 mouse fibroblast in order to determine the biocompatibility. After a 2-day incubation, the aerogels with high Cu^{2+} concentration (>12 mg/L) resulted in no cell survival. However, a lower concentration of Cu^{2+} in the aerogels showed a similar growth of cells when compared to the control cells. Microbial studies showed inhibition of E. coli growth for all Cu containing aerogels. This indicated that the antimicrobial property of copper remained when composited into this aerogel. Another study investigated chitosan aerogels for wound healing applications [204]. Chitosan hydrogels were supercritically dried with CO_2. Vancomycin, an antibiotic, was loaded into the chitosan solution prior to becoming a gel. Collagenase, a protein that is active in collagen degradation and remodeling after injury, was studied in relation to chitosan aerogel particles. After a 4-h incubation of chitosan aerogels in a collagenase medium, it was found that there was no effect in the performance of the collagenase; thus, the chitosan aerogels

are expected to not inhibit the normal healing process. Antimicrobial studies against *Staphylococcus aureus* were also investigated. Vancomycin-loaded chitosan aerogel particles were able to eliminate 98% of the bacterial culture within 6 h and 100% after 48 h. Cell viability studies showed 80% cell viability after 24 h. In another study, hybrid aerogels were formed from collagen and reinforced with wheat grass [205]. Collagen is an extracellular matrix protein that has been used in tissue engineering applications based on its cell recognition signals, controllable mechanical properties, and biodegradability [206]. Wheat grass extract was introduced to collagen to overcome its poor susceptibility of proteolytic degradation, microbial attacks and allow crosslinking of collagen fibrils. The aerogel was fabricated by mixing goat tendon collagen with wheat grass extract in phosphate buffer saline. The solution was then incubated at 37 °C for 1 h under UV light at pH 7.2. The resulting gel was washed and frozen at −80 °C and lyophilized. Various collage-wheat grass aerogels were fabricated with different concentration of wheat grass including 0, 1, 2, 3% (*w/v*). The cytocompatibility studies revealed an increase in cell growth compared to the control for 1 and 2% collagen-wheat grass aerogels. Chorio allantoic membrane assay was performed to study the angiogenic activity of the aerogels; the study demonstrated that growth of blood vessels in the wheat grass reinforced aerogels compared to collagen aerogels without wheat grass. Wound healing assays were performed on female wistar rats using the collagen aerogels compared to the collagen wheat grass aerogels for 18 days. The study showed a higher reduction in wound size in collagen-wheat grass aerogels compared to collagen aerogels, on day 9 there was a reduction of the size of 75% for the wheat grass reinforced aerogel compared to 47% reduction of collagen aerogel (Figure 19).
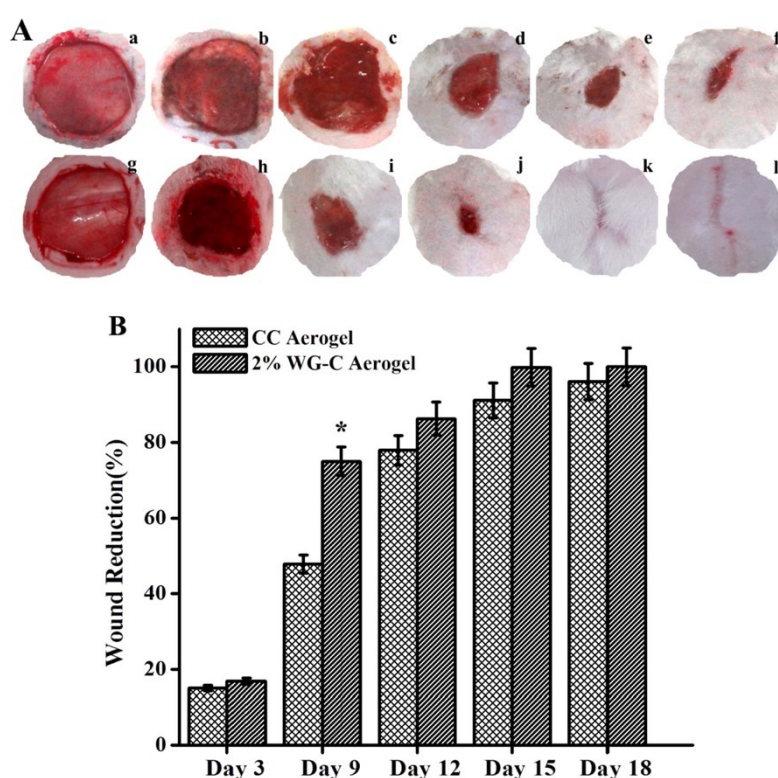
Figure 19. (**A**) Wound healing study where a–f (top row) show the collagen control aerogel at day 0, 3, 9, 12, 15, and 18 and g–l (bottom row) show the 12% collagen-wheat grass aerogel at day 0, 3, 9, 12, 15, and 18. Image (**B**) shows the wound healing as a percent of wound reduction. Adapted from [205] with permission, copyright American Chemical Society, 2017.

5. Summary and Perspectives

Aerogels have been extensively investigated for various applications due to their high porosities, high specific surface area, and ultralow densities, aiding in the creation of novel lightweight yet highly

functional structures. Incorporating nanomaterials into aerogels improved their mechanical stability and strength, and introduces unique functionalities such as high electrical conductivities, thermal stability, and reactivity. Recently, many strategies have been explored towards the development of novel aerogel-based composite systems containing interesting and high-performing nanomaterials. The advance of aerogels includes developing production methods, using novel nanomaterials and exploring novel applications.

While supercritical drying used to be the state-of-the-art method for aerogel fabrication, a variety of methods such as freeze-drying and 3D-printing have been developed to produce aerogels. In contrast to the high-pressure and high-temperature process of supercritical drying, freeze-drying is a lower-cost, more simple technique that uses the formation of an ice crystal to dictate the porous structure of the aerogel, though some shrinkage and cracking can occur. 3D-printing is another aerogel fabrication method that is revolutionizing the field. 3D-printing can create highly complex structures using three different processing techniques: stereolithography, inkjet printing, and direct ink writing, but is limited by the requirement of specific types of print materials, costly equipment, and production efficacy. Therefore, more effort will be devoted in formulating appropriate ink for 3D-printing aerogels.

1D nanomaterials such as CNTs, nanofibers, cellulose have been used as the framework of the aerogel or as one of the aerogel components. Nanocellulose is an abundant and renewable biopolymer derived from various plant, animal, and bacteria sources. Cellulose appears in two different forms (i.e., cellulose nanocrystals and cellulose nanofiber), each with different structural properties, but high potential for surface modifications. Nanofibers are thread-like nanomaterials in which dispersions of single nanofibers or fiber mats can be dried to create nanofibrous aerogels with enhanced specific surface area and networked framework. They also are versatile in fabrication and application due to the wide polymer and inorganic material selection, adaptable processing techniques, and the coupling/functionalization with other nanostructures and compounds. Carbon nanotubes function as components and spacers in aerogel composites to improve the structural and mechanical properties, as well as to promote electrical conductivity.

2D nanomaterials are also being extensively studied to be used as components in the aerogel composites. Graphene is of great interest in aerogel synthesis due to its unique nanostructure that offers great mechanical, physical, and chemical properties. It also has excellent electrical and thermal conductivity, but poor solvent dispersibility. Its derivative, graphene oxide, is commonly used to form a graphene aerogel as it can be dispersed in solvents without aggregation. It is then reduced to partially restore its graphitic network and reinstate these outstanding material properties within the aerogel construct. Additionally, the usage of polymers or other nanomaterials can aid to prevent or minimize the stacking of graphene oxide sheets, providing a better stable framework. 2D nanomaterials other than graphene have also been investigated to be incorporated into aerogels, for example, inorganic boron nitride and molybdenum disulfide. These materials are usually deposited on graphene or carbon nanotube aerogels through CVD. More cost-effective fabrication methods are needed to extend their applications.

Nanomaterial-incorporating aerogel composites are being developed to be used in applications in various fields. Firstly, the aerogel composites can be designed for environmental applications. Hydrophobic aerogel composites can be created from hydrophobic polymers and surfactants as well as surface and chemical modification and can be used as porous sorbents for oil spills. The porosity of the aerogel, along with the incorporation of electrically conductive nanomaterials such as CNTs, carbon nanofibers, graphene, and other inorganic 2D nanomaterials, leads to the possibility of designing aerogels for energy storage applications like supercapacitors and lithium ion batteries. Biomedical applications, such as for drug delivery, tissue scaffolds and wound healing, can benefit from aerogel composites owing to the high loading capacity from the porosity and specific surface area and usage of biocompatible aerogel materials.

It is obvious that nanomaterials have granted aerogels a variety of properties, including robust mechanical properties, flexibility, electrical conductivity that are not available for bulk aerogels.

It is expected that more nanomaterials with unique properties will be used in aerogel fabrication. For example, 2D materials beyond graphene will be added in 3D-printing inks to produce aerogels with complex 3D structures. Nanomaterials with high capacitance of charges or lithium ions are required to produce flexible aerogels for the application in energy storage devices. In addition, more rational design of aerogel structures as demonstrated by Duan and coworkers will be further pursued to introduce improved properties into aerogels.

Author Contributions: All authors contributed equally to the preparation of the manuscript.

Conflicts of Interest: The authors declare no conflict of interest.

References

1. Araby, S.; Qiu, A.; Wang, R.; Zhao, Z.; Wang, C.H.; Ma, J. Aerogels based on carbon nanomaterials. *J. Mater. Sci.* **2016**, *51*, 9157–9189. [CrossRef]
2. Pierre, A.C. History of Aerogels. In *Aerogels Handbook. Advances in Sol-Gel Derived Materials and Technologies*; Aegerter, M., Leventis, N., Koebel, M., Eds.; Springer: New York, NY, USA, 2011; pp. 3–18.
3. Zhang, M.; Fang, S.; Zakhidov, A.A.; Lee, S.B.; Alieve, A.E.; Williams, C.D.; Atkinson, K.R.; Baughman, R.H. Strong, transparent, multifunctinoal, carbon nanotube sheets. *Science* **2005**, *209*, 1215–1220. [CrossRef] [PubMed]
4. Mohanan, J.L.; Arachchige, I.U.; Brock, S.L. Porous semiconductor chalcogenide aerogels. *Science* **2005**, *307*, 397–400.
5. Elam, J.W.; Xiong, G.; Han, C.Y.; Wang, H.H.; Birrell, J.P.; Welp, U.; Hryn, J.N.; Pellin, M.J.; Baumann, T.F.; Poco, J.F.; et al. Atomic layer deposition for the conformal coating of nanoporous materials. *J. Nanomater.* **2006**, *2006*, 1–5. [CrossRef]
6. Gurav, J.L.; Jung, I.K.; Park, H.H.; Kang, E.S.; Nadargi, D.Y. Silica aerogel: Synthesis and applications. *J. Nanomater.* **2010**, *2010*, 23. [CrossRef]
7. Hüsing, N.; Schubert, U. Aerogels—Airy Materials: Chemistry, Structure, and Properties. *Angew. Chem. Int. Ed.* **1998**, *37*, 22–45. [CrossRef]
8. Capadona, L.A.; Meador, M.A.B.; Alunni, A.; Fabrizio, E.F.; Vassilaras, P.; Leventis, N. Flexible, low-density polymer crosslinked silica aerogels. *Polymer* **2006**, *47*, 5754–5761. [CrossRef]
9. Leventis, N.; Lu, H. Polymer-Crosslinked Aerogels. In *Aerogels Handbook. Advances in Sol-Gel Derived Materials and Technologies*; Aegerter, M., Leventis, N., Koebel, M., Eds.; Springer: New York, NY, USA, 2011; pp. 251–285.
10. Hench, L.L.; West, J.K. The sol-gel process. *Chem. Rev.* **1990**, *90*, 33–72. [CrossRef]
11. Mulik, S.; Sotiriou-leventis, C.; Leventis, N. Time-Efficient Acid-Catalyzed Synthesis of Resorcinol—Formaldehyde Aerogels. *Chem. Mater.* **2007**, *19*, 6138–6144. [CrossRef]
12. Zhang, J.; Cao, Y.; Feng, J.; Wu, P. Graphene-oxide-sheet-induced gelation of cellulose and promoted mechanical properties of composite aerogels. *J. Phys. Chem. C* **2012**, *116*, 8063–8068. [CrossRef]
13. Hdach, H.; Woignier, T.; Phalippou, J.; Scherer, G.W. Effect of aging and pH on the modulus of aerogels. *J. Non. Cryst. Solids* **1990**, *121*, 202–205. [CrossRef]
14. Einarsrud, M.; Nilsen, E.; Rigacci, A.; Pajonk, G.M.; Buathier, S. Strengthening of silica gels and aerogels by washing and aging processes. *J. Non-Cryst. Solids* **2001**, *285*, 1–7. [CrossRef]
15. Soleimani Dorcheh, A.; Abbasi, M.H. Silica aerogel; synthesis, properties and characterization. *J. Mater. Process. Technol.* **2008**, *199*, 10–26. [CrossRef]
16. Hæreid, S.; Anderson, J.; Einarsrud, M.A.; Hua, D.W.; Smith, D.M. Thermal and temporal aging of TMOS-based aerogel precursors in water. *J. Non-Cryst. Solids* **1995**, *185*, 221–226. [CrossRef]
17. Omranpour, H.; Motahari, S. Effects of processing conditions on silica aerogel during aging: Role of solvent, time and temperature. *J. Non-Cryst. Solids* **2013**, *379*, 7–11. [CrossRef]
18. Cheng, C.-P.; Iacobucci, P.A. Inorganic Oxide Aerogels and Their Preparation. U.S. Patent 4,717,708, 5 January 1988.
19. Beckman, E.J. Supercritical or near-critical CO_2 in green chemical synthesis and processing. *J. Supercrit. Fluids* **2004**, *28*, 121–191. [CrossRef]

20. Jin, H.; Nishiyama, Y.; Wada, M.; Kuga, S. Nanofibrillar cellulose aerogels. *Colloids Surfaces A Physicochem. Eng. Asp.* **2004**, *240*, 63–67. [CrossRef]

21. Jiménez-Saelices, C.; Seantier, B.; Cathala, B.; Grohens, Y. Effect of freeze-drying parameters on the microstructure and thermal insulating properties of nanofibrillated cellulose aerogels. *J. Sol-Gel Sci. Technol.* **2017**, *84*, 475–485. [CrossRef]

22. Wang, C.; Chen, X.; Wang, B.; Huang, M.; Wang, B.; Jiang, Y.; Ruoff, R.S. Freeze-Casting Produces a Graphene Oxide Aerogel with a Radial and Centrosymmetric Structure. *ACS Nano* **2018**, *12*, 5816–5825. [CrossRef]

23. Simon-Herrero, C.; Caminero-Huertas, S.; Romero, A.; Valverde, J.L.; Sanchez-Silva, L. Effects of freeze-drying conditions on aerogel properties. *J. Mater. Sci.* **2016**, *51*, 8977–8985. [CrossRef]

24. Deville, S. Ice-templating, freeze casting: Beyond materials processing. *J. Mater. Res.* **2013**, *28*, 2202–2219. [CrossRef]

25. Deville, S. The lure of ice-templating: Recent trends and opportunities for porous materials. *Scr. Mater.* **2018**, *147*, 119–124. [CrossRef]

26. Shen, C.; Calderon, J.E.; Barrios, E.; Soliman, M.; Khater, A.; Jeyaranjan, A.; Tetard, L.; Gordon, A.; Seal, S.; Zhai, L. Anisotropic electrical conductivity in polymer derived ceramics induced by graphene aerogels. *J. Mater. Chem. C* **2017**, *5*, 11708–11716. [CrossRef]

27. Ali, I.; Chen, L.; Huang, Y.; Song, L.; Lu, X.; Liu, B.; Zhang, L.; Zhang, J.; Hou, L.; Chen, T. Humidity-Responsive Gold Aerogel for Real-Time Monitoring of Human Breath. *Langmuir* **2018**, *34*, 4908–4913. [CrossRef]

28. Cong, L.; Li, X.; Ma, L.; Peng, Z.; Yang, C.; Han, P.; Wang, G.; Li, H.; Song, W.; Song, G. High-performance graphene oxide/carbon nanotubes aerogel-polystyrene composites: Preparation and mechanical properties. *Mater. Lett.* **2018**, *214*, 190–193. [CrossRef]

29. Cao, N.; Lyu, Q.; Li, J.; Wang, Y.; Yang, B.; Szunerits, S.; Boukherroub, R. Facile synthesis of fluorinated polydopamine/chitosan/reduced graphene oxide composite aerogel for efficient oil/water separation. *Chem. Eng. J.* **2017**, *326*, 17–28. [CrossRef]

30. Jia, J.; Wang, C. A facile restructuring of 3D high water absorption aerogels from methoxy polyethylene glycol-polycaprolactone (mPEG-PCL) nanofibers. *Mater. Sci. Eng. C* **2019**, *94*, 965–975. [CrossRef]

31. Zhang, Q.; Zhang, F.; Xu, X.; Zhou, C.; Lin, D. Three-dimensional printing hollow polymer template-mediated graphene lattices with tailorable architectures and multifunctinoal properties. *ACS Nano* **2018**, *12*, 1096–1106. [CrossRef]

32. Tang, X.; Zhu, C.; Cheng, D.; Zhou, H.; Liu, X.; Xie, P.; Zhao, Q.; Zhang, D.; Fan, T. Architectured leaf-inspired $Ni_{0.33}Co_{0.66}S_2$/graphene aerogels via 3D printing for high-performance energy storage. *Adv. Funct. Mater.* **2018**, *28*, 1805057. [CrossRef]

33. Ambrosi, A.; Pumera, M. 3D-printing technologies for electrochemical applications. *Chem. Soc. Rev.* **2016**, *45*, 2740–2755. [CrossRef]

34. Zhu, C.; Liu, T.; Qian, F.; Chen, W.; Chandrasekara, S.; Yao, B.; Song, Y.; Duoss, E.B.; Kuntz, J.D.; Spadaccini, C.M.; et al. 3D printed functional nanomaterials for electrochemical energy storage. *Nano Today* **2017**, *15*, 107–120. [CrossRef]

35. Farahani, R.D.; Dubé, M.; Therriault, D. Three-Dimensional Printing of Multifunctional Nanocomposites: Manufacturing Techniques and Applications. *Adv. Mater.* **2016**, *28*, 5794–5821. [CrossRef]

36. Dizon, J.R.C.; Espera, A.H.; Chen, Q.; Advincula, R.C. Mechanical characterization of 3D-printed polymers. *Addit. Manuf.* **2018**, *20*, 44–67. [CrossRef]

37. Zhang, F.; Wei, M.; Viswanathan, V.V.; Swart, B.; Shao, Y.; Wu, G.; Zhou, C. 3D printing technologies for electrochemical energy storage. *Nano Energy* **2017**, *40*, 418–431. [CrossRef]

38. Saeed, S.; Al-Sobaihi, R.M.; Bertino, M.F.; White, L.S.; Saoud, K.M. Laser induced instantaneous gelation: Aerogels for 3D printing. *J. Mater. Chem. A* **2015**, *3*, 17606–17611. [CrossRef]

39. White, L.S.; Selden, T.; Bertino, M.F.; Cartin, C.; Angello, J.; Schwan, M.; Milow, B.; Ratke, L. Fabrication of Mechanically Strong Honeycombs with Aerogel Cores. *Ind. Eng. Chem. Res.* **2018**, *57*, 1197–1206. [CrossRef]

40. Iijima, S. Helical microtubules of graphitic carbon. *Nature* **1991**, *354*, 56–58. [CrossRef]

41. Nardecchia, S.; Carriazo, D.; Ferrer, M.L.; Gutiérrez, M.C.; del Monte, F. Three dimensional macroporous architectures and aerogels built of carbon nanotubes and/or graphene: Synthesis and applications. *Chem. Soc. Rev.* **2013**, *42*, 794–830. [CrossRef]

42. Frank, S.; Poncharal, P.; Wang, Z.L.; De Heer, W.A. Carbon nanotube quantum resistors. *Science* **1998**, *280*, 1744–1746. [CrossRef]

43. Wei, B.Q.; Vajtai, R.; Ajayan, P.M. Reliability and current carrying capacity of carbon nanotubes. *Appl. Phys. Lett.* **2001**, *79*, 1172–1174. [CrossRef]

44. Liang, W.; Bockrath, M.; Bozovic, D.; Hafner, J.H.; Tinkham, M.; Park, H. Fabry-Perot interference in a nanotube electron waveguide. *Nature* **2001**, *411*, 665–669. [CrossRef] [PubMed]

45. Liu, C.; Cheng, H.-M. Controlled Growth of Semiconducting and Metallic Single-Wall Carbon Nanotubes. *J. Am. Chem. Soc.* **2016**, *138*, 6690–6698. [CrossRef] [PubMed]

46. Kim, S.H.; Mulholland, G.W.; Zachariah, M.R. Density measurement of size selected multiwalled carbon nanotubes by mobility-mass characterization. *Carbon N. Y.* **2009**, *47*, 1297–1302. [CrossRef]

47. Yu, M.-F.; Lourie, O.; Dyer, M.J.; Moloni, K.; Kelly, T.F.; Ruoff, R.S. Strength and Breaking Mechanism of Multiwalled Carbon Nanotubes Under Tensile Load. *Science* **2000**, *287*, 637–640. [CrossRef]

48. Kis, A.; Zettl, A. Nanomechanics of carbon nanotubes. *Philos. Trans. R. Soc. A Math. Phys. Eng. Sci.* **2008**, *366*, 1591–1611. [CrossRef] [PubMed]

49. Datsyuk, V.; Kalyva, M.; Papagelis, K.; Parthenios, J.; Tasis, D.; Siokou, A.; Kallitsis, I.; Galiotis, C. Chemical oxidation of multiwalled carbon nanotubes. *Carbon N. Y.* **2008**, *46*, 833–840. [CrossRef]

50. Cao, A.; Dickrell, P.L.; Sawyer, W.G.; Ghasemi-Nejhad, M.N.; Ajayan, P.M. Materials science: Super-compressible foamlike carbon nanotube films. *Science* **2005**, *310*, 1307–1310. [CrossRef] [PubMed]

51. Liu, Y.; Kumar, S. Polymer/carbon nanotube nano composite fibers-A review. *ACS Appl. Mater. Interfaces* **2014**, *6*, 6069–6087. [CrossRef] [PubMed]

52. Khare, K.S.; Khabaz, F.; Khare, R. Effect of carbon nanotube functionalization on mechanical and thermal properties of cross-linked epoxy-carbon nanotube nanocomposites: Role of strengthening the interfacial interactions. *ACS Appl. Mater. Interfaces* **2014**, *6*, 6098–6110. [CrossRef] [PubMed]

53. Vaisman, L.; Wagner, H.D.; Marom, G. The role of surfactants in dispersion of carbon nanotubes. *Adv. Colloid Interface Sci.* **2006**, *128–130*, 37–46. [CrossRef]

54. Lv, P.; Tan, X.W.; Yu, K.H.; Zheng, R.L.; Zheng, J.J.; Wei, W. Super-elastic graphene/carbon nanotube aerogel: A novel thermal interface material with highly thermal transport properties. *Carbon N. Y.* **2016**, *99*, 222–228. [CrossRef]

55. Bryning, M.B.; Milkie, D.E.; Islam, M.F.; Hough, L.A.; Kikkawa, J.M.; Yodh, A.G. Carbon nanotube aerogels. *Adv. Mater.* **2007**, *19*, 661–664. [CrossRef]

56. Zou, J.; Liu, J.; Karakoti, A.S.; Kumar, A.; Joung, D.; Li, Q.; Khondaker, S.I.; Seal, S.; Zhai, L. Ultralight Multiwalled Carbon Nanotube Aerogel. *ACS Nano* **2010**, *4*, 7293–7302. [CrossRef]

57. Ai, L.; Jiang, J. Removal of methylene blue from aqueous solution with self-assembled cylindrical graphene-carbon nanotube hybrid. *Chem. Eng. J.* **2012**, *192*, 156–163. [CrossRef]

58. De Marco, M.; Markoulidis, F.; Menzel, R.; Bawaked, S.M.; Mokhtar, M.; Al-Thabaiti, S.A.; Basahel, S.N.; Shaffer, M.S.P. Cross-linked single-walled carbon nanotube aerogel electrodes: Via reductive coupling chemistry. *J. Mater. Chem. A* **2016**, *4*, 5385–5389. [CrossRef]

59. Zhu, Z.; Yao, H.; Dong, J.; Qian, Z.; Dong, W.; Long, D. High-mechanical-strength polyimide aerogels crosslinked with 4, 4′-oxydianiline-functionalized carbon nanotubes. *Carbon N. Y.* **2019**, *144*, 24–31. [CrossRef]

60. Shin, S.J.; Kucheyev, S.O.; Worsley, M.A.; Hamza, A. V Mechanical deformation of carbon-nanotube-based aerogels. *Carbon N. Y.* **2012**, *50*, 5340–5342. [CrossRef]

61. Zhan, W.; Gao, L.; Fu, X.; Siyal, S.H.; Sui, G.; Yang, X. Green synthesis of amino-functionalized carbon nanotube-graphene hybrid aerogels for high performance heavy metal ions removal. *Appl. Surf. Sci.* **2019**, *467–468*, 1122–1133. [CrossRef]

62. Li, Y.; Zhao, M.; Chen, J.; Fan, S.; Liang, J.; Ding, L.; Chen, S. Flexible chitosan/carbon nanotubes aerogel, a robust matrix for in-situ growth and non-enzymatic biosensing applications. *Sens. Actuators B Chem.* **2016**, *232*, 750–757. [CrossRef]

63. Gao, L.; Wang, F.; Zhan, W.; Wang, Y.; Sui, G.; Yang, X. Viable synthesis of highly compressible, ultra-light graphene-carbon nanotube composite aerogels without additional reductant and their applications for strain-sensitivity. *Chem. Commun.* **2017**, *53*, 521–524. [CrossRef]

64. Li, Y.; Liu, X.; Nie, X.; Yang, W.; Wang, Y.; Yu, R.; Shui, J. Multifunctional Organic-Inorganic Hybrid Aerogel for Self-Cleaning, Heat-Insulating, and Highly Efficient Microwave Absorbing Material. *Adv. Funct. Mater.* **2019**, *29*, 1807624. [CrossRef]

65. Liu, Y.; Su, Y.; Guan, J.; Cao, J.; Zhang, R.; He, M.; Jiang, Z. Asymmetric Aerogel Membranes with Ultrafast Water Permeation for the Separation of Oil-in-Water Emulsion. *ACS Appl. Mater. Interfaces* **2018**, *10*, 26546–26554. [CrossRef] [PubMed]

66. Hu, H.; Zhao, Z.; Gogotsi, Y.; Qiu, J. Compressible Carbon Nanotube-Graphene Hybrid Aerogels with Superhydrophobicity and Superoleophilicity for Oil Sorption. *Environ. Sci. Technol. Lett.* **2014**, *1*, 214–220. [CrossRef]

67. Wan, W.; Zhang, R.; Li, W.; Liu, H.; Lin, Y.; Li, L.; Zhou, Y. Graphene-carbon nanotube aerogel as an ultra-light, compressible and recyclable highly efficient absorbent for oil and dyes. *Environ. Sci. Nano* **2016**, *3*, 107–113. [CrossRef]

68. Gao, Q.; Jin, Y.; Jin, Y.; Wang, X.; Ye, Z.; Hong, Z.; Zhi, M. Synthesis of amorphous MoSxand MoSx/carbon nanotubes composite aerogels as effective hydrogen evolution reaction catalysts. *J. Sol-Gel Sci. Technol.* **2018**, *88*, 227–235. [CrossRef]

69. Liu, T.; Mai, X.; Chen, H.; Ren, J.; Liu, Z.; Li, Y.; Gao, L.; Wang, N.; Zhang, J.; He, H.; et al. Carbon nanotube aerogel-CoS 2 hybrid catalytic counter electrodes for enhanced photovoltaic performance dye-sensitized solar cells. *Nanoscale* **2018**, *10*, 4194. [CrossRef]

70. Ye, Y.; Bindl, D.J.; Jacobberger, R.M.; Wu, M.Y.; Roy, S.S.; Arnold, M.S. Semiconducting carbon nanotube aerogel bulk heterojunction solar cells. *Small* **2014**, *10*, 3299–3306. [CrossRef] [PubMed]

71. Pääkkö, M.; Vapaavuori, J.; Silvennoinen, R.; Kosonen, H.; Ankerfors, M.; Lindström, T.; Berglund, L.A.; Ikkala, O. Long and entangled native cellulose i nanofibers allow flexible aerogels and hierarchically porous templates for functionalities. *Soft Matter* **2008**, *4*, 2492–2499. [CrossRef]

72. Long, L.Y.; Weng, Y.X.; Wang, Y.Z. Cellulose aerogels: Synthesis, applications, and prospects. *Polymers* **2018**, *8*, 623. [CrossRef] [PubMed]

73. Wu, Z.-Y.; Liang, H.-W.; Hu, B.-C.; Yu, S.-H. Emerging Carbon Nanofiber Aerogels: Chemosynthesis versus Biosynthesis. *Angew. Chem. Int. Ed.* **2018**, *57*, 15646–15662. [CrossRef] [PubMed]

74. Way, A.E.; Hsu, L.; Shanmuganathan, K.; Weder, C.; Rowan, S.J. PH-responsive cellulose nanocrystal gels and nanocomposites. *ACS Macro Lett.* **2012**, *1*, 1001–1006. [CrossRef]

75. Kargarzadeh, H.; Huang, J.; Lin, N.; Ahmad, I.; Mariano, M.; Dufresne, A.; Thomas, S.; Gałęski, A. Recent developments in nanocellulose-based biodegradable polymers, thermoplastic polymers, and porous nanocomposites. *Prog. Polym. Sci.* **2018**, *87*, 197–227. [CrossRef]

76. Beck-Candanedo, S.; Roman, M.; Gray, D.G. Effect of reaction conditions on the properties and behavior of wood cellulose nanocrystal suspensions. *Biomacromolecules* **2005**, *6*, 1048–1054. [CrossRef] [PubMed]

77. Gupta, P.; Singh, B.; Agrawal, A.K.; Maji, P.K. Low density and high strength nanofibrillated cellulose aerogel for thermal insulation application. *Mater. Des.* **2018**, *158*, 224–236. [CrossRef]

78. Nguyen, B.N.; Cudjoe, E.; Douglas, A.; Scheiman, D.; McCorkle, L.; Meador, M.A.B.; Rowan, S.J. Polyimide Cellulose Nanocrystal Composite Aerogels. *Macromolecules* **2016**, *49*, 1692–1703. [CrossRef]

79. Cudjoe, E.; Hunsen, M.; Xue, Z.; Way, A.E.; Barrios, E.; Olson, R.A.; Hore, M.J.A.; Rowan, S.J. Miscanthus Giganteus: A commercially viable sustainable source of cellulose nanocrystals. *Carbohydr. Polym.* **2017**, *155*, 230–241. [CrossRef]

80. Salas, C.; Nypelö, T.; Rodriguez-Abreu, C.; Carrillo, C.; Rojas, O.J. Nanocellulose properties and applications in colloids and interfaces. *Curr. Opin. Colloid Interface Sci.* **2014**, *19*, 383–396. [CrossRef]

81. Hees, T.; Zhong, F.; Rudolph, T.; Walther, A.; Mülhaupt, R. Nanocellulose Aerogels for Supporting Iron Catalysts and In Situ Formation of Polyethylene Nanocomposites. *Adv. Funct. Mater.* **2017**, *27*, 1–8. [CrossRef]

82. Wang, W.; Sun, Y.; Liu, B.; Wang, S.; Cao, M. Porous carbon nanofiber webs derived from bacterial cellulose as an anode for high performance lithium ion batteries. *Carbon* **2015**, *91*, 56–65. [CrossRef]

83. Esa, F.; Tasirin, S.M.; Rahman, N.A. Overview of Bacterial Cellulose Production and Application. *Agric. Agric. Sci. Procedia* **2014**, *2*, 113–119. [CrossRef]

84. Chen, W.; Yu, H.; Lee, S.Y.; Wei, T.; Li, J.; Fan, Z. Nanocellulose: A promising nanomaterial for advanced electrochemical energy storage. *Chem. Soc. Rev.* **2018**, *47*, 2837–2872. [CrossRef]

85. De Oliveira, J.P.; Bruni, G.P.; Fabra, M.J.; da Rosa Zavareze, E.; López-Rubio, A.; Martínez-Sanz, M. Development of food packaging bioactive aerogels through the valorization of Gelidium sesquipedale seaweed. *Food Hydrocoll.* **2019**, *89*, 337–350. [CrossRef]

86. Li, J.; Zuo, K.; Wu, W.; Xu, Z.; Yi, Y.; Jing, Y.; Dai, H.; Fang, G. Shape memory aerogels from nanocellulose and polyethyleneimine as a novel adsorbent for removal of Cu(II) and Pb(II). *Carbohydr. Polym.* **2018**, *196*, 376–384. [CrossRef]

87. Fiorati, A.; Turco, G.; Travan, A.; Caneva, E.; Pastori, N.; Cametti, M.; Punta, C.; Melone, L. Mechanical and drug release properties of sponges from cross-linked cellulose nanofibers. *Chempluschem* **2017**, *82*, 848–858. [CrossRef]

88. Liu, J.; Cheng, F.; Grénman, H.; Spoljaric, S.; Seppälä, J.; Eriksson, J.E.; Willför, S.; Xu, C. Development of nanocellulose scaffolds with tunable structures to support 3D cell culture. *Carbohydr. Polym.* **2016**, *148*, 259–271. [CrossRef]

89. Zu, G.; Shen, J.; Zou, L.; Wang, F.; Wang, X.; Zhang, Y.; Yao, X. Nanocellulose-derived highly porous carbon aerogels for supercapacitors. *Carbon N. Y.* **2016**, *99*, 203–211. [CrossRef]

90. Li, V.C.F.; Dunn, C.K.; Zhang, Z.; Deng, Y.; Qi, H.J. Direct Ink Write (DIW) 3D Printed Cellulose Nanocrystal Aerogel Structures. *Sci. Rep.* **2017**, *7*, 1–8. [CrossRef] [PubMed]

91. Li, V.C.F.; Mulyadi, A.; Dunn, C.K.; Deng, Y.; Qi, H.J. Direct Ink Write 3D Printed Cellulose Nanofiber Aerogel Structures with Highly Deformable, Shape Recoverable, and Functionalizable Properties. *ACS Sustain. Chem. Eng.* **2018**, *6*, 2011–2022. [CrossRef]

92. Håkansson, K.M.O.; Henriksson, I.C.; de la Peña Vázquez, C.; Kuzmenko, V.; Markstedt, K.; Enoksson, P.; Gatenholm, P. Solidification of 3D Printed Nanofibril Hydrogels into Functional 3D Cellulose Structures. *Adv. Mater. Technol.* **2016**, *1*, 1600096. [CrossRef]

93. Bhardwaj, N.; Kundu, S.C. Electrospinning: A Fascinating Fiber Fabrication Technique. *Biotechnol. Adv.* **2010**, *28*, 325–347. [CrossRef]

94. Reneker, D.H.; Yarin, A.L. Electrospinning jets and polymer nanofibers. *Polymer* **2008**, *49*, 2387–2425. [CrossRef]

95. Ondarcuhu, T.; Joachim, C. Drawing a single nanofibre over hundreds of microns. *Europhys. Lett.* **1998**, *42*, 215–220. [CrossRef]

96. Hulteen, J.C.; Chen, H.X.; Chambliss, C.K.; Martin, C.R. Template synthesis of carbon nanotubule and nanofiber arrays. *Nanostruct. Mater.* **1997**, *9*, 133–136. [CrossRef]

97. Hartgerink, J.D.; Beniash, E.; Stupp, S.I. Self-assembly and mineralization of peptide-amphiphile nanofibers. *Science* **2001**, *294*, 1684–1688. [CrossRef]

98. Zhang, Z.; Tu, W.; Peijs, T.; Bastiaansen, C.W.M. Fabrication and properties of poly(tetrafluoroethylene) nanofibres via sea-island spinning. *Polymer* **2017**, *109*, 321–331. [CrossRef]

99. Zhang, X.; Lu, Y. Centrifugal spinning: An alternative approach to fabricate nanofibers at high speed and low cost. *Polym. Rev.* **2014**, *54*, 677–701. [CrossRef]

100. Medeiros, E.S.; Glenn, G.M.; Klamczynski, A.P.; Orts, W.J.; Mattoso, L.H.C. Solution Blow Spinning: A New Method to Produce Micro- and Nanofibers from Polymer Solutions. *J. Appl. Polym. Sci.* **2009**, *113*, 2322–2330. [CrossRef]

101. Teo, W.E.; Inai, R.; Ramakrishna, S. Technological advances in electrospinning of nanofibers. *Sci. Technol. Adv. Mater.* **2011**, *12*, 013002. [CrossRef]

102. Deuber, F.; Mousavi, S.; Federer, L.; Hofer, M.; Adlhart, C. Exploration of Ultralight Nanofiber Aerogels as Particle Filters: Capacity and Efficiency. *ACS Appl. Mater. Interfaces* **2018**, *10*, 9069. [CrossRef]

103. Si, Y.; Wang, X.; Dou, L.; Yu, J.; Ding, B. Ultralight and fire-resistant ceramic nanofibrous aerogels with temperature-invariant superelasticity. *Sci. Adv.* **2018**, *4*, eaas8925. [CrossRef]

104. Si, Y.; Yu, J.; Tang, X.; Ge, J.; Ding, B. Ultralight nanofibre-assembled cellular aerogels with superelasticity and multifunctionality. *Nat. Commun.* **2014**, *5*, 5802. [CrossRef] [PubMed]

105. Mašek, O. Biochar in thermal and thermochemical biorefineries-production of biochar as a coproduct. In *Handbook of Biofuels Production: Processes and Technologies*, 2nd ed.; Woodhead Publishing: Cambridge, MA, USA, 2016; pp. 655–671.

106. Qian, H.S.; Yu, S.H.; Luo, L.B.; Gong, J.Y.; Fei, L.F.; Liu, X.M. Synthesis of uniform Te@carbon-rich composite nanocables with photoluminescence properties and carbonaceous nanofibers by the hydrothermal carbonization of glucose. *Chem. Mater.* **2006**, *18*, 2102–2108. [CrossRef]

107. Song, L.T.; Wu, Z.Y.; Liang, H.W.; Zhou, F.; Yu, Z.Y.; Xu, L.; Pan, Z.; Yu, S.H. Macroscopic-scale synthesis of nitrogen-doped carbon nanofiber aerogels by template-directed hydrothermal carbonization of nitrogen-containing carbohydrates. *Nano Energy* **2016**, *19*, 117–127. [CrossRef]

108. Liang, H.W.; Wang, L.; Chen, P.Y.; Lin, H.T.; Chen, L.F.; He, D.; Yu, S.H. Carbonaceous nanofiber membranes for selective filtration and separation of nanoparticles. *Adv. Mater.* **2010**, *22*, 4691–4695. [CrossRef] [PubMed]

109. Novoselov, K.S.; Geim, A.K.; Morozov, S.V.; Jiang, D.; Zhang, Y.; Dubonos, S.V.; Grigorieva, I.V.; Firsov, A.A. Electric Field Effect in Atomically Thin Carbon Films. *Science* **2004**, *306*, 666–669. [CrossRef]

110. Morozov, S.V.; Novoselov, K.S.; Katsnelson, M.I.; Schedin, F.; Elias, D.C.; Jaszczak, J.A.; Geim, A.K. Giant intrinsic carrier mobilities in graphene and its bilayer. *Phys. Rev. Lett.* **2008**, *100*, 11–14. [CrossRef] [PubMed]

111. Balandin, A.A. Thermal properties of graphene and nanostructured carbon materials. *Nat. Mater.* **2011**, *10*, 569–581. [CrossRef]

112. Stankovich, S.; Dikin, D.A.; Dommett, G.H.B.; Kohlhaas, K.M.; Zimney, E.J.; Stach, E.A.; Piner, R.D.; Nguyen, S.B.T.; Ruoff, R.S. Graphene-based composite materials. *Nature* **2006**, *442*, 282–286. [CrossRef] [PubMed]

113. Lee, C.; Wei, X.; Kysar, J.W.; Hone, J. Measurement of the Elastic Properties and Intrinsic Strength of Monolayer Graphene. *Science* **2008**, *321*, 385–389. [CrossRef] [PubMed]

114. Dreyer, D.R.; Park, S.; Bielawski, C.W.; Ruoff, R.S. The chemistry of graphene oxide. *Chem. Soc. Rev.* **2009**, *39*, 228–240. [CrossRef] [PubMed]

115. Stankovich, S.; Dikin, D.A.; Piner, R.D.; Kohlhaas, K.A.; Kleinhammes, A.; Jia, Y.; Wu, Y.; Nguyen, S.T.; Ruoff, R.S. Synthesis of graphene-based nanosheets via chemical reduction of exfoliated graphite oxide. *Carbon N. Y.* **2007**, *45*, 1558–1565. [CrossRef]

116. Gao, W. (Ed.) Spectroscopy and Microscopy of Graphene Oxide and Reduced Graphene Oxide. In *Graphene Oxide: Reduction Recipes, Spectroscopy, and Applications*; Springer International Publishing: Cham, Switzerland, 2015; pp. 1–24.

117. Zhang, Y.; Huang, Y.; Yang, G.; Bu, F.; Li, K.; Shakir, I.; Xu, Y. Dispersion-Assembly Approach to Synthesize Three-Dimensional Graphene/Polymer Composite Aerogel as a Powerful Organic Cathode for Rechargeable Li and Na Batteries. *ACS Appl. Mater. Interfaces* **2017**, *9*, 15549–15556. [CrossRef] [PubMed]

118. Li, R.; Chen, C.; Li, J.; Xu, L.; Xiao, G.; Yan, D. A facile approach to superhydrophobic and superoleophilic graphene/polymer aerogels. *J. Mater. Chem. A* **2014**, *2*, 3057. [CrossRef]

119. Hong, J.Y.; Bak, B.M.; Wie, J.J.; Kong, J.; Park, H.S. Reversibly compressible, highly elastic, and durable graphene aerogels for energy storage devices under limiting conditions. *Adv. Funct. Mater.* **2015**, *25*, 1053–1062. [CrossRef]

120. Wu, X.; Tang, L.; Zheng, S.; Huang, Y.; Yang, J.; Liu, Z.; Yang, W.; Yang, M. Hierarchical unidrectional graphen aerogel/polyaniline composite for high performance supercapacitors. *J. Power Sources* **2018**, *397*, 189–195. [CrossRef]

121. Han, Q.; Yang, L.; Liang, Q.; Ding, M. Three-dimensional hierarchical porous graphene aerogel for efficient adsorption and preconcentration of chemical warfare agents. *Carbon N. Y.* **2017**, *122*, 556–563. [CrossRef]

122. Xiao, J.; Lv, W.; Xie, Z.; Song, Y.; Zheng, Q. graphene oxide/poly (vinyl alcohol) ultralight aerogel as a broad-spectrum adsorbent for anionic and cationic dyes L -cysteine-reduced. *J. Mater. Sci.* **2017**, *52*, 5807–5821. [CrossRef]

123. Shen, C.; Barrios, E.; Mcinnis, M.; Zuyus, J.; Zhai, L. Fabrication of Graphene Aerogels with Heavily Loaded Metallic Nanoparticles. *Micromachines* **2017**, *8*, 47. [CrossRef]

124. Hu, X.; Xu, W.; Zhou, L.; Tan, Y.; Wang, Y.; Zhu, S. Tailoring Graphene Oxide-Based Aerogels for Efficient Solar Steam Generation under One Sun. *Adv. Mater.* **2017**, *29*, 1604031. [CrossRef] [PubMed]

125. Zuo, L.; Fan, W.; Zhang, Y.; Zhang, L.; Gao, W.; Huang, Y.; Liu, T. Graphene/montmorillonite hybrid synergistically reinforced polyimide composite aerogels with enhanced fl ame-retardant performance. *Compos. Sci. Technol.* **2017**, *139*, 57–63. [CrossRef]

126. Wei, X.; Huang, T.; Yang, J.; Zhang, N.; Wang, Y.; Zhou, Z. Green synthesis of hybrid graphene oxide/microcrystalline cellulose aerogels and their use as superabsorbents. *J. Hazard. Mater.* **2017**, *335*, 28–38. [CrossRef] [PubMed]

127. Chen, Y.; Zhang, H.; Wang, M.; Qian, X.; Dasari, A.; Yu, Z. Phenolic resin-enhanced three-dimensional graphene aerogels and their epoxy nanocomposites with high mechanical and electromagnetic interference shielding performances. *Compos. Sci. Technol.* **2017**, *152*, 254–262. [CrossRef]

128. Cao, D.; Cing, Y.; Tantratian, K.; Wang, X.; Ma, Y.; Mukhopadhyay, A.; Cheng, Z.; Zhang, Q.; Jiao, Y.; Chen, L.; et al. 3D printed high-performance lithium metal microbatteries enabled by nanocellulose. *Adv. Mater.* **2019**, *31*, 1807313. [CrossRef] [PubMed]

129. Wei, M.; Zhang, F.; Wang, W.; Alexandridis, P.; Zhou, C.; Wu, G. 3D direct writing fabrication of electrodes for electrochemical storage devices. *J. Power Sources* **2017**, *354*, 134–147. [CrossRef]

130. Zhu, C.; Han, T.Y.J.; Duoss, E.B.; Golobic, A.M.; Kuntz, J.D.; Spadaccini, C.M.; Worsley, M.A. Highly compressible 3D periodic graphene aerogel microlattices. *Nat. Commun.* **2015**, *6*, 6962. [CrossRef] [PubMed]

131. Zhang, Q.; Zhang, F.; Medarametla, S.P.; Li, H.; Zhou, C.; Lin, D. 3D Printing of Graphene Aerogels. *Small* **2016**, *12*, 1702–1708. [CrossRef]

132. Ashton, M.; Paul, J.; Sinnott, S.B.; Hennig, R.B. Topology-Scaling Identification of Layered Solid and Stable Exfoliated 2D Materials. *Phys. Rev. Lett.* **2017**, *118*, 10601. [CrossRef] [PubMed]

133. Worsley, M.A.; Shin, S.J.; Merrill, M.D.; Lenhardt, J.; Nelson, A.J.; Woo, L.Y.; Gash, A.E.; Baumann, T.F.; Orme, C.A. Ultralow Density, Monolithic WS 2, MoS 2, and MoS 2/Graphene Aerogels. *ACS Nano* **2015**, *9*, 4698–4705. [CrossRef] [PubMed]

134. Long, H.; Harley-Trochimczyk, A.; Pham, T.; Zettle, A.; Tang, Z.; Shi, T.; Carraro, C.; Worsley, M.A.; Maboudian, R. High surface area 3D MoS2/Graphene Hybrid Aerogel for Ultrasensitive NO2 Detection. *Adv. Funct. Mater.* **2016**, *26*, 5158–5165. [CrossRef]

135. Tang, X.; Zhou, H.; Cai, Z.; Cheng, D.; He, P.; Xie, P.; Zhang, D.; Fan, T. Generalized 3D Printing of Graphene-Based Mixed-Dimensional Hybrid Aerogels. *ACS Nano* **2018**, *12*, 3502–3511. [CrossRef] [PubMed]

136. Lee, J.H.; Park, N.; Kim, B.G.; Jung, D.S.; Im, K.; Hur, J.; Choi, J.W. Restacking-inhibited 3D reduced graphene oxide for high performance supercapacitor electrodes. *ACS Nano* **2013**, *7*, 9366–9374. [CrossRef]

137. Joo Jeong, Y.; Islam, M.F. Compressibl elastomeric aerogels of hexagonal boron nitride and sinlge-walled carbon nanotubes. *Nanoscale* **2015**, *7*, 12888–12894. [CrossRef] [PubMed]

138. Xu, X.; Zhang, Q.; Hao, M.; Hu, Y.; Lin, Z.; Peng, L.; Wang, T.; Ren, X.; Wang, C.; Zhao, Z.; et al. Double-negative-index ceramic aerogels for thermal superinsulation. *Science* **2019**, *363*, 723–727. [CrossRef] [PubMed]

139. Xu, X.; Zhang, Q.; Yu, Y.; Chen, W.; Hu, H.; Li, H. Naturally dried graphene aerogels with superelasticity and tunable poisson's ratio. *Adv. Mater.* **2016**, *28*, 9223–9230. [CrossRef] [PubMed]

140. Maleki, H. Recent advances in aerogels for environmental remediation applications: A review. *Chem. Eng. J.* **2016**, *300*, 98–118. [CrossRef]

141. Boday, D.J.; Stover, R.J.; Muriithi, B.; Loy, D.A. Strong, low density, hexylene- and phenylene-bridged polysilsesquioxane aerogel-polycyanoacrylate composites. *J. Mater. Sci.* **2011**, *46*, 6371–6377. [CrossRef]

142. Cheng, H.; Gu, B.; Pennefather, M.P.; Nguyen, T.X.; Phan-Thien, N.; Duong, H.M. Cotton aerogels and cotton-cellulose aerogels from environmental waste for oil spillage cleanup. *Mater. Des.* **2017**, *130*, 452–458. [CrossRef]

143. Duan, Y.; Jana, S.C.; Lama, B.; Espe, M.P. Hydrophobic silica aerogels by silylation. *J. Non-Cryst. Solids* **2016**, *437*, 26–33. [CrossRef]

144. Li, R.; Li, A.; Zheng, T.; Lu, L.; Gao, Y. Hydrophobic and flexible cellulose aerogel as an efficeint, green and resuable ion sorbent. *RSC Adv.* **2015**, *5*, 82027–82033.

145. Zu, G.; Kanamori, K.; Maeno, A.; Kaji, H.; Nakanishi, K. Superflexible Multifunctional Polyvinylpoly dimethylsiloxane-Based Aerogels as Efficient Absorbents, Thermal Superinsulators, and Strain Sensors. *Angew. Chem. Int. Ed.* **2018**, *57*, 9722–9727. [CrossRef]

146. Maleki, H.; Whitmore, L.; Hüsing, N. Novel multifunctional polymethylsilsesquioxane-silk fibroin aerogel hybrids for environmental and thermal insulation applications. *J. Mater. Chem. A* **2018**, *6*, 12598–12612. [CrossRef] [PubMed]

147. Madyan, O.A.; Fan, M. Hydrophobic clay aerogel composites through the implantation of environmentally friendly water-repellent agents. *Macromolecules* **2018**, *51*, 10113–10120. [CrossRef]

148. Xu, Z.; Jiang, X.; Zhou, H.; Li, J. Preparation of magnetic hydrophobic polyvinyl alcohol (PVA)-cellulose nanofiber (CNF) aerogels as effective oil absorbents. *Cellulose* **2018**, *25*, 1217–1227. [CrossRef]

149. Ma, Q.; Liu, Y.; Dong, Z.; Wang, J.; Hou, X. Hydrophobic and nanoporous chitosan-silica composite aerogels for oil absorption. *J. Appl. Polym. Sci.* **2015**, *132*, 1–11. [CrossRef]

150. Zhou, S.; Jiang, W.; Wang, T.; Lu, Y. Highly Hydrophobic, Compressible, and Magnetic Polystyrene/Fe3O4 Graphene Aerogel Composite for Oil-Water Separation. *Ind. Eng. Chem. Res.* **2015**, *54*, 5460–5467. [CrossRef]

151. Jung, H.N.R.; Lee, Y.K.; Parale, V.G.; Cho, H.H.; Mahadik, D.B.; Park, H.H. Hydrophobic silica composite aerogels using poly(methyl methacrylate) by rapid supercritical extraction process. *J. Sol-Gel Sci. Technol.* **2017**, *83*, 692–697. [CrossRef]

152. Zhang, X.; Wang, H.; Cai, Z.; Yan, N.; Liu, M.; Yu, Y. Highly compressible and hydrophobic anisotropic aerogels for selective oil/organic solvent absorption. *ACS Sustain. Chem. Eng.* **2019**, *7*, 332–340. [CrossRef]

153. Karatum, O.; Steiner, S.A.; Griffin, J.S.; Shi, W.; Plata, D.L. Flexible, Mechanically Durable Aerogel Composites for Oil Capture and Recovery. *ACS Appl. Mater. Interfaces* **2016**, *8*, 215–224. [CrossRef]

154. Aghajamali, M.; Xie, H.; Javadi, M.; Kalisvaart, W.P.; Buriak, J.M.; Veinot, J.G.C. Size and surface effects of silicon nanocrystals in graphene aerogel compoiste anodes for lithium ion batteries. *Chem. Mater.* **2018**, *30*, 7782–7792. [CrossRef]

155. Jiang, L.; Lin, B.; Li, X.; Song, X.; Xia, H.; Li, L.; Zeng, H. Monolayer MoS2-Graphene Hybrid Aerogels with Controllable Porosity for Lithium-Ion Batteries with High Reversible Capacity. *ACS Appl. Mater. Interfaces* **2016**, *8*, 2680–2687. [CrossRef]

156. Zhang, X.; Lin, Z.; Chen, B.; Zhang, W.; Sharma, S.; Gu, W.; Deng, Y. Solid-state flexible polyaniline/silver cellulose nanofibrils aerogel supercapacitors. *J. Power Sources* **2014**, *246*, 283–289. [CrossRef]

157. Conway, B.E. Transition from "Supercapacitor" to "Battery" Behavior in Electrochemical Energy Storage. *J. Electrochem. Soc.* **1991**, *138*, 1539–1548. [CrossRef]

158. Yang, F.; Xu, M.; Bao, S.-J.; Wei, H.; Chai, H. Self-assembled hierarchical graphene/polyaniline hybrid aerogels for electrochemical capacitive energy storage. *Electrochim. Acta* **2014**, *137*, 381–387. [CrossRef]

159. Van Hoa, N.; Quyen, T.T.H.; Van Hieu, N.; Ngoc, T.Q.; Thinh, P.V.; Dat, P.A.; Nguyen, H.T.T. Three-dimensional reduced graphene oxide-grafted polyaniline aerogel as an active material for high performance supercapacitors. *Synth. Met.* **2017**, *223*, 192–198. [CrossRef]

160. Han, S.; Wu, D.; Li, S.; Zhang, F.; Feng, X. Porous graphene materials for advanced electrochemical energy storage and conversion devices. *Adv. Mater.* **2014**, *26*, 849–864. [CrossRef]

161. Mao, J.; Iocozzia, J.; Huang, J.; Meng, K.; Lai, Y.; Lin, Z. Graphene aerogels for efficient energy storage and conversion. *Energy Environ. Sci.* **2018**, *11*, 772–799. [CrossRef]

162. Yang, Z.; Tian, J.; Yin, Z.; Cui, C.; Qian, W.; Wei, F. Carbon nanotube- and graphene-based nanomaterials and applications in high-voltage supercapacitor: A review. *Carbon N. Y.* **2019**, *141*, 467–480. [CrossRef]

163. Borenstein, A.; Hanna, O.; Attias, R.; Luski, S.; Brousse, T.; Aurbach, D. Carbon-based composite materials for supercapacitor electrodes: A review. *J. Mater. Chem. A* **2017**, *5*, 12653–12672. [CrossRef]

164. Yu, M.; Han, Y.; Li, J.; Wang, L. Magnetic N-doped carbon aerogel from sodium carboxymethyl cellulose/collagen composite aerogel for dye adsorption and electrochemical supercapacitor. *Int. J. Biol. Macromol.* **2018**, *115*, 185–193. [CrossRef]

165. Yang, X.; Shi, K.; Zhitomirsky, I.; Cranston, E.D. Cellulose Nanocrystal Aerogels as Universal 3D Lightweight Substrates for Supercapacitor Materials. *Adv. Mater.* **2015**, *27*, 6104–6109. [CrossRef]

166. Yang, X.; Fei, B.; Ma, J.; Liu, X.; Yang, S.; Tian, G.; Jiang, Z. Porous nanoplatelets wrapped carbon aerogels by pyrolysis of regenerated bamboo cellulose aerogels as supercapacitor electrodes. *Carbohydr. Polym.* **2018**, *180*, 385–392. [CrossRef]

167. Yu, Z.; McInnis, M.; Calderon, J.; Seal, S.; Zhai, L.; Thomas, J. Functionalized graphene aerogel composites for high-performance asymmetric supercapacitors. *Nano Energy* **2015**, *11*, 611–620. [CrossRef]

168. Sun, R.; Chen, H.; Li, Q.; Song, Q.; Zhang, X. Spontaneous assembly of strong and conductive graphene/polypyrrole hybrid aerogels for energy storage. *Nanoscale* **2014**, *6*, 12912–12920. [CrossRef]

169. Lin, H.; Huang, Q.; Wang, J.; Jiang, J.; Liu, F.; Chen, Y.; Wang, C.; Lu, D.; Han, S. Self-Assembled Graphene/Polyaniline/Co3O4 Ternary Hybrid Aerogels for Supercapacitors. *Electrochim. Acta* **2016**, *191*, 444–451. [CrossRef]

170. Shao, Q.; Tang, J.; Lin, Y.; Li, J.; Qin, F.; Yuan, J.; Qin, L.C. Carbon nanotube spaced graphene aerogels with enhanced capacitance in aqueous and ionic liquid electrolytes. *J. Power Sources* **2015**, *278*, 751–759. [CrossRef]

171. Zhou, G.; Kim, N.R.; Chun, S.E.; Lee, W.; Um, M.K.; Chou, T.W.; Islam, M.F.; Byun, J.H.; Oh, Y. Highly porous and easy shapeable poly-dopamine derived graphene-coated single walled carbon nanotube aerogels for stretchable wire-type supercapacitors. *Carbon N. Y.* **2018**, *130*, 137–144. [CrossRef]

172. Gao, Z.; Yang, J.; Huang, J.; Xiong, C.; Yang, Q. A three-dimensional graphene aerogel containing solvent-free polyaniline fluid for high performance supercapacitors. *Nanoscale* **2017**, *9*, 17710–17716. [CrossRef] [PubMed]

173. Niu, Q.; Guo, Y.; Gao, K.; Shao, Z. Polypyrrole/cellulose nanofiber aerogel as a supercapacitor electrode material. *RSC Adv.* **2016**, *6*, 109143–109149. [CrossRef]

174. Qi, Z.; Ye, J.; Chen, W.; Biener, J.; Duoss, E.B.; Spadaccini, C.M.; Worsley, M.A.; Zhu, C. 3D-Printed, Superelastic Polypyrrole-Graphene Electrodes with Ultrahigh Areal Capacitance for Electrochemical Energy Storage. *Adv. Mater. Technol.* **2018**, *3*, 1800053. [CrossRef]

175. He, J.; Li, P.; Lv, W.; Wen, K.; Chen, Y.; Zhang, W.; Li, Y.; Qin, W.; He, W. Three-dimensional hierarchically structured aerogels constructed with layered MoS2/graphene nanosheets as free-standing anodes for high-performance lithium ion batteries. *Electrochim. Acta* **2016**, *215*, 12–18. [CrossRef]

176. Qiu, B.; Xing, M.; Zhang, J. Mesoporous TiO2 nanocrystals grown in situ on graphene aerogels for high photocalysis and lithium-ion batteries. *J. Am. Chem. Soc.* **2014**, *136*, 5852–5855. [CrossRef] [PubMed]

177. Wan, Y.; Yang, Z.; Xiong, G.; Luo, H. A general strategy of decorating 3D carbon nanofiber aerogels derived from bacterial cellulose with nano-Fe3O4 for high-performance flexible and binder-free lithium-ion battery anodes. *J. Mater. Chem. A* **2015**, *3*, 15386–15393. [CrossRef]

178. Huang, Y.; Lin, Z.; Zheng, M.; Wang, T.; Yang, J.; Yuan, F.; Lu, X.; Liu, L.; Sun, D. Amorphous Fe2O3nanoshells coated on carbonized bacterial cellulose nanofibers as a flexible anode for high-performance lithium ion batteries. *J. Power Sources* **2016**, *307*, 649–656. [CrossRef]

179. Liao, H.; Zhang, H.; Hong, H.; Li, Z.; Qin, G.; Zhu, H.; Lin, Y. Novel cellulose aerogel coated on polypropylene separators as gel polymer electrolyte with high ionic conductivity for lithium-ion batteries. *J. Membr. Sci.* **2016**, *514*, 332–339. [CrossRef]

180. Wan, J.; Zhang, J.; Yu, J.; Zhang, J. Cellulose Aerogel Membranes with a Tunable Nanoporous Network as a Matrix of Gel Polymer Electrolytes for Safer Lithium-Ion Batteries. *ACS Appl. Mater. Interfaces* **2017**, *9*, 24591–24599. [CrossRef] [PubMed]

181. Li, M.; Carter, R.; Douglas, A.; Oakes, L.; Pint, C.L. Sulfur Vapor-Infiltrated 3D Carbon Nanotube Foam for Binder-Free High Areal Capacity Lithium-Sulfur Battery Composite Cathodes. *ACS Nano* **2017**, *11*, 4877–4884. [CrossRef] [PubMed]

182. Xu, J.; Xin, S.; Liu, J.; Wang, J.; Lei, Y.; Yu, S. Elastic Carbon Nanotube Aerogel Meets Tellurium Nanowires: A Binder- and Collector-Free Electrode for Li-Te Batteries. *Adv. Funct. Mater.* **2016**, 3580–3588. [CrossRef]

183. Kong, D.; Li, X.; Zhang, Y.; Hai, X.; Wang, B.; Qiu, X.; Song, Q.; Yang, Q.; Zhi, L. Encapsulating V2O5 into carbon nanotubes enables the synthesis of flexible high-performance lithium-ion batteries. *Energy Environ. Sci.* **2016**, *9*, 906–911. [CrossRef]

184. Chen, Y.M.; Yu, X.; Yu, X.Y.; Li, Z.; Paik, U.; Lou, X.W. Hierarchical MoS2 tubular structure internally wired by carbon nanotubes as a highly stable anode material for lithium-ion batteries. *Sci. Adv.* **2016**, *2*, e1600021. [CrossRef]

185. Gu, D.; Li, W.; Wang, F.; Bongard, H.; Spliethoff, B.; Schmidt, W.; Weidenthaler, C.; Xia, Y.; Zhoa, D.; Schuth, F. Controllable synthesis of mesopourous peadpod-like Co3O4@carbon nanotube arrays for high-performance lithium-ion batteries. *Angew. Chem.* **2015**, *54*, 7060–7064. [CrossRef]

186. Gao, H.; Zhou, T.; Zheng, Y.; Yuqing, L.; Chen, J.; Liu, H.; Guo, Z. Integrated carbon/red phosphorous/graphene aerogel 3D architecture via advanced vapor-redistribution for high-energy sodium-ion batteries. *Adv. Energy Mater.* **2016**, *6*, 1601037. [CrossRef]

187. Bang, A.; Buback, C.; Sotiriou-Leventis, C.; Leventis, N. Flexible aerogels from hyperbranched polyurethanes: Probing the role of molecular rigidity with poly(Urethane Acrylates) versus poly(Urethane Norbornenes). *Chem. Mater.* **2014**, *26*, 6979–6993. [CrossRef]

188. Mao, Y.; Li, G.; Guo, Y.; Li, Z.; Liang, C.; Peng, X.; Lin, Z. Foldable interpenetrated metal-organic frameworks/carbon nanotubes thin film for lithium-sulfur batteries. *Nat. Commun.* **2017**, *8*, 1–8. [CrossRef] [PubMed]

189. Xu, F.; Jin, S.; Zhong, H.; Wu, D.; Yang, X.; Chen, X.; Wei, H.; Fu, R.; Jiang, D. Electrochemically active, crystalline, mesoporous covalent organic frameworks on carbon nanotubes for synergistic lithium-ion battery energy storage. *Sci. Rep.* **2015**, *5*, 1–6. [CrossRef] [PubMed]

190. Salgado, M.; Santos, F.; Rodríguez-Rojo, S.; Reis, R.L.; Duarte, A.R.C.; Cocero, M.J. Development of barley and yeast β-glucan aerogels for drug delivery by supercritical fluids. *J. CO2 Util.* **2017**, *22*, 262–269. [CrossRef]

191. Mallepally, R.R.; Marin, M.A.; Surampudi, V.; Subia, B.; Rao, R.R.; Kundu, S.C.; McHugh, M.A. Silk fibroin aerogels: Potential scaffolds for tissue engineering applications. *Biomed. Mater.* **2015**, *10*, 035002. [CrossRef] [PubMed]

192. Weng, L.; Boda, S.K.; Wang, H.; Teusink, M.J.; Shuler, F.D.; Xie, J. Novel 3D Hybrid Nanofiber Aerogels Coupled with BMP-2 Peptides for Cranial Bone Regeneration. *Adv. Healthc. Mater.* **2018**, *7*, 1–16. [CrossRef]

193. Jia, H.; Tian, Q.; Xu, J.; Lu, L.; Ma, X.; Yu, Y. Aerogels prepared from polymeric β-cyclodextrin and graphene aerogels as a novel host-guest system for immobilization of antibodies: A voltammetric immunosensor for the tumor marker CA 15–3. *Microchim. Acta* **2018**, *185*, 517. [CrossRef]

194. Shao, L.; Cao, Y.; Li, Z.; Hu, W.; Li, S.; Lu, L. Dual responsive aerogel made from thermo/pH sensitive graft copolymer alginate-g-P(NIPAM-co-NHMAM) for drug controlled release. *Int. J. Biol. Macromol.* **2018**, *114*, 1338–1344. [CrossRef]

195. Mehling, T.; Smirnova, I.; Guenther, U.; Neubert, R.H.H. Polysaccharide-based aerogels as drug carriers. *J. Non-Cryst. Solids* **2009**, *355*, 2472–2479. [CrossRef]

196. Ulker, Z.; Erkey, C. An emerging platform for drug delivery: Aerogel based systems. *J. Control. Release* **2014**, *177*, 51–63. [CrossRef] [PubMed]

197. Hans, M.L.; Lowman, A.M. Lowman Biodegradable nanoparticles for drug delivery and targeting. *Curr. Opin. Solid State Mater. Sci.* **2002**, *6*, 319–327. [CrossRef]

198. Zhao, J.; Lu, C.; He, X.; Zhang, X.; Zhang, W.; Zhang, X. Polyethylenimine-grafted cellulose nanofibril aerogels as versatile vehicles for drug delivery. *ACS Appl. Mater. Interfaces* **2015**, *7*, 2607–2615. [CrossRef]

199. Bugnone, C.A.; Ronchetti, S.; Manna, L.; Banchero, M. An emulsification/internal setting technique for the preparation of coated and uncoated hybrid silica/alginate aerogel beads for controlled drug delivery. *J. Supercrit. Fluids* **2018**, *142*, 1–9. [CrossRef]

200. López-Iglesias, C.; Casielles, A.M.; Altay, A.; Bettini, R.; Alvarez-Lorenzo, C.; García-González, C.A. From the printer to the lungs: Inkjet-printed aerogel particles for pulmonary delivery. *Chem. Eng. J.* **2019**, *357*, 559–566. [CrossRef]

201. Quraishi, S.; Martins, M.; Barros, A.A.; Gurikov, P.; Raman, S.P.; Smirnova, I.; Duarte, A.R.C.; Reis, R.L. Novel non-cytotoxic alginate–lignin hybrid aerogels as scaffolds for tissue engineering. *J. Supercrit. Fluids* **2015**, *105*, 1–8. [CrossRef]

202. Vallachira Warriam Sasikumar, P.; Zera, E.; Graczyk-Zajac, M.; Riedel, R.; Soraru, G.D.; Dunn, B. Structural Design of Polymer-Derived SiOC Ceramic Aerogels for High-Rate Li Ion Storage Applications. *J. Am. Ceram. Soc.* **2016**, *99*, 2977–2983. [CrossRef]

203. Wang, X.; Cheng, F.; Liu, J.; Smått, J.H.; Gepperth, D.; Lastusaari, M.; Xu, C.; Hupa, L. Biocomposites of copper-containing mesoporous bioactive glass and nanofibrillated cellulose: Biocompatibility and angiogenic promotion in chronic wound healing application. *Acta Biomater.* **2016**, *46*, 286–298. [CrossRef]

204. López-Iglesias, C.; Barros, J.; Ardao, I.; Monteiro, F.J.; Alvarez-Lorenzo, C.; Gómez-Amoza, J.L.; García-González, C.A. Vancomycin-loaded chitosan aerogel particles for chronic wound applications. *Carbohydr. Polym.* **2019**, *204*, 223–231. [CrossRef]

205. Govindarajan, D.; Duraipandy, N.; Srivatsan, K.V.; Lakra, R.; Korapatti, P.S.; Jayavel, R.; Kiran, M.S. Fabrication of Hybrid Collagen Aerogels Reinforced with Wheat Grass Bioactives as Instructive Scaffolds for Collagen Turnover and Angiogenesis for Wound Healing Applications. *ACS Appl. Mater. Interfaces* **2017**, *9*, 16939–16950. [CrossRef]

206. Sorushanova, A.; Delgado, L.M.; Wu, Z.; Shologu, N.; Kshirsagar, A.; Raghunath, R.; Mullen, A.M.; Bayon, Y.; Pandit, A.; Raghunath, M.; et al. The Collagen Suprafamily: From Biosynthesis to Advanced Biomaterial Development. *Adv. Mater.* **2019**, *31*, 1801651.